

Upper crustal seismic structure of the Endeavour Segment, Juan de Fuca Ridge from travel time tomography: Implications for oceanic crustal accretion

Robert T. Weekly¹, William S.D. Wilcock², Douglas R. Toomey³, Emilie E.E. Hooft³, Eunyoung Kim⁴

(1) Department of Earth and Space Sciences, University of Washington, Box 351310, Seattle, WA 98195-1310

(2) School of Oceanography, University of Washington, Box 357940, Seattle, WA 98195-7940

(3) Department of Geological Sciences, University of Oregon, 1272 University of Oregon, Eugene, OR 97403-1272

(4) School of Earth and Environmental Sciences, Seoul National University, Seoul, Korea, Republic of

This article has been accepted for publication and undergone full peer review but has not been through the copyediting, typesetting, pagination and proofreading process which may lead to differences between this version and the Version of Record. Please cite this article as doi: 10.1002/2013GC005159

Abstract

The isotropic and anisotropic P -wave velocity structure of the upper oceanic crust on the Endeavour Segment of the Juan de Fuca Ridge is studied using refracted travel time data collected by an active-source, three-dimensional tomography experiment. The isotropic velocity structure is characterized by low crustal velocities in the overlapping spreading centers (OSCs) at the segment ends. These low velocities are indicative of pervasive tectonic fracturing and persist off-axis, recording the history of ridge propagation. Near the segment center, velocities within the upper 1 km show ridge-parallel bands with low velocities on the outer flanks of topographic highs. These features are consistent with localized thickening of the volcanic extrusive layer from eruptions extending outside of the axial valley that flow down the fault-tilted blocks that form the abyssal hill topography. On-axis velocities are generally relatively high beneath the hydrothermal vent fields likely due to the infilling of porosity by mineral precipitation. Lower velocities are observed beneath the most vigorous vent fields in a seismically active region above the axial magma chamber and may reflect increased fracturing and higher temperatures. Seismic anisotropy is high on-axis but decreases substantially off-axis over 5-10 km (0.2-0.4 Ma). This decrease coincides with an increase in seismic velocities resolved at depths ≥ 1 km and is attributed to the infilling of cracks by mineral precipitation associated with near-axis hydrothermal circulation. The orientation of the fast-axis of anisotropy is ridge-parallel near the segment center but curves near the segment ends reflecting the tectonic fabric within the OSCs.

1. Introduction

The upper oceanic crust is formed by episodic diking and eruptive volcanic events sourced from mid-crustal magma chambers, and is subsequently modified by tectonic extension, hydrothermal alteration, and off-axis volcanism. Understanding the interplay of these processes and their variation with time and location is an important goal of mid-ocean ridge research. Because seismic velocities are sensitive to composition, porosity, fracturing, temperature and the presence of melt, marine seismic imaging techniques are useful tools for characterizing the structure of the crustal accretion zone and the off-axis crustal stratigraphy that reflects the time-integrated history of upper oceanic crust.

Marine refraction tomography constrains spatial variations in seismic velocity and is thus complementary to multichannel seismic (MCS) studies [e.g., *Kent et al.*, 1990; *Hooft et al.*,

1997] that image interfaces in seismic properties and shallow velocity structure. At mid-ocean ridges tomographic studies have measured: (1) thickness variations in layer 2A inferred from velocity variations within the upper 1 km of crust [Hussenoeder *et al.*, 1996; Singh *et al.*, 1998]; (2) variations in the upper crust related to fracturing and thermal structure [Harding *et al.*, 1993; Kent *et al.*, 1994; Kappus *et al.*, 1995; Carbotte *et al.*, 1997]; (3) mid-crustal magma bodies located both beneath the ridge axis [Toomey *et al.*, 1990; Dunn *et al.*, 2000; Magde *et al.*, 2000] and away from it [Durant and Toomey, 2009]; and (4) variations in anisotropy that are directly related to aligned cracks and fractures in the upper crust [Sohn *et al.*, 1997; Barclay *et al.*, 1998; Dunn and Toomey, 2001; Barclay and Wilcock, 2004; Tong *et al.*, 2004; Seher *et al.*, 2010b].

The Endeavour segment of the Juan de Fuca Ridge (JdFR) has an intermediate spreading rate and is characterized by a central portion underlain by an axial magma chamber (AMC) that supports several high-temperature hydrothermal vent fields and by large overlapping spreading centers at either end. In this study, we utilize seismic tomographic methods to characterize three-dimensional segment-scale variations in the isotropic and anisotropic velocity structure of the upper crust of the Endeavour segment. The images are used to investigate the processes of crustal accretion and their variations along-axis on an intermediate spreading rate ridge segment.

2. Geologic Setting

The Endeavour segment is a ~90-km long, intermediate-rate (52 mm/yr full-spreading rate [DeMets *et al.*, 2010]) spreading center located near the northern end of the JdFR (Figure 1). It forms left-stepping overlapping spreading centers (OSCs) with the West Valley and Northern Symmetric segments. To the south, the Cobb OSC separates the Endeavour and Northern Symmetric segments by ~30 km. Since its formation at 5 Ma [Hey and Wilson, 1982] the net migration of the Cobb OSC has been to the north, but it has undergone alternating episodes of northward and southward propagation during its recent history [Johnson *et al.*, 1983; Shoberg *et al.*, 1991]. From 0.7 – 0.4 Ma the northern end of the Northern Symmetric segment propagated quickly northward leaving a bathymetric record of a failed propagator on the Juan de Fuca Plate (Figure 1). The southern end of the Endeavour segment then propagated more gradually to the south before the current episode of northward propagation of the Northern Symmetric segment started at < 0.1 Ma [Shoberg *et al.*, 1991]. To the north, the Endeavour – West Valley (E-WV)

OSC separates the two spreading centers by 15 km. The E-WV OSC formed within the past 50 kyr, and perhaps as recently as 10 kyr, when the spreading axis switched from the Middle Valley segment to the West Valley segment (Figure 1) as a result of ongoing reorganization of plate boundaries at the northern end of the Juan de Fuca Ridge [Davis and Lister, 1977; Davis and Villinger, 1992].

Several prominent seamount chains on the Pacific plate side of the JdFR intersect the Endeavour segment [Davis and Karsten, 1986]; they are, from south to north, the Springfield, Heckle, and Heck seamount chains (Figure 1). The central 20 km portion of the Endeavour segment features a plateau that extends 45 km across axis and is elevated 300 m relative to the rest of the segment. It has been postulated that this plateau is a result of enhanced crustal production due to the ridge capturing the hot spot anomaly associated with the Heckle Seamount chain [Karsten and Delaney, 1989; Carbotte et al., 2008].

A recent MCS experiment indicates that AMCs underlie portions of each segment of the JdFR. The thickness of seismic layer 2A and the AMC depth vary by segment [Carbotte et al., 2008] and, in general, both increase from south to north. On the Endeavour segment, the AMC underlies the central portion of the segment at 2.1 – 3.3 km depth [Van Ark et al., 2007]. The AMC provides a heat source for five high temperature hydrothermal vent fields that are 2 – 3 km apart in the axial valley [Kelley et al., 2002; 2012]. From south to north, the fields are named Mothra, Main Endeavour, High Rise, Salty Dawg, and Sasquatch. The hydrothermal systems have been studied extensively and are characterized by significant along-axis gradients in temperature and chemistry [Butterfield et al., 1994; Kelley et al., 2002; 2012].

Studies of microearthquakes from the central axial region show a concentration of seismicity at ~2-km depth just above the AMC [Wilcock et al., 2002; 2009; Weekly et al., 2013], with the most intense seismicity occurring beneath the High Rise and Main Endeavour fields [Wilcock et al., 2009] which also have the largest area and highest heat flux [Kellogg, 2011]. McClain et al. [1993] argue that off-axis normal faults maintain the conduits necessary to support robust hydrothermal circulation and the formation of long-standing vent fields. The characteristics of hypocenters and focal mechanisms for earthquakes recorded in 2003-2004 are consistent with ongoing magma inflation [Wilcock et al., 2009].

The Endeavour segment has been the site of several large volcanic earthquake swarms. In June 1999, a swarm on the central Endeavour [Johnson et al., 2000; Bohnenstiehl et al., 2004]

significantly perturbed the chemistry of hydrothermal fluids [Lilley *et al.*, 2003; Seyfried *et al.*, 2003] and was the result of a dike intrusion [Davis *et al.*, 2001]. A second swarm to south in the 2000 may also have been associated with a dike [Bohnenstiehl *et al.*, 2004]. In January and February 2005, two complex seismic swarm sequences located near the E-WV OSC likely involved magmatic intrusions on the northern Endeavour and southernmost portion of the West Valley segment [Hooft *et al.*, 2010; Weekly *et al.*, 2013]. These swarms were followed by a substantial decrease in seismicity rates along the Endeavour segment and have been interpreted as the end of a 6-year non-eruptive spreading event that started with the 1999 swarms and cumulatively relieved plate-spreading stresses [Weekly *et al.*, 2013].

The MCS data show that seismic layer 2A thickens along axis from about 150 – 300 m at the northern end of the Endeavour segment to almost 600 m at the southern end [Van Ark *et al.*, 2007]. In contrast to seismic studies conducted at the southern JdFR [Canales *et al.*, 2005] and the East Pacific Rise [Harding *et al.*, 1993; Kent *et al.*, 1994] that found evidence for 2A thickness increasing off-axis, there is no clear pattern of off-axis thickening at the Endeavour segment [Van Ark *et al.*, 2007]. There appears to be a weak correlation between fault-bounded, axis-parallel bathymetric highs and a thicker layer 2A [Van Ark *et al.*, 2007]. Barclay and Wilcock [2004] also inferred this correlation from a small seismic refraction data set. MCS profiles that extend onto the flanks of the JdFR show systematic increases in layer 2 velocities with off-axis distance; layer 2A velocities increase rapidly near axis and then more gradually on the flanks, attaining values typical for mature oceanic crust of ~4.0 km/s within 5 – 8 Ma of formation [Nedimovic *et al.*, 2008]. The upper portion of layer 2B undergoes a rapid maturation with velocities increasing by ~0.8 km/s within ~0.5 Ma [Newman *et al.*, 2011]. The rapid evolution of layers 2A and 2B is attributed to mineral precipitation driven by the solidification and cooling of the oceanic crust, while the more gradual evolution of layer 2A well off axis results from a reduction in porosity of the upper extrusive volcanic unit through long-term exposure to “passive” off-axis hydrothermal circulation [Carbotte *et al.*, 2012].

3. Experiment Geometry and Data Acquisition

In August and September 2009, a three-dimensional seismic tomography experiment was conducted along the Endeavour segment (Figure 2). A seismic network comprising 68 four-component (three orthogonal geophones and a hydrophone) ocean bottom seismometers (OBSs)

was deployed at 64 sites and recorded ~5,500 airgun shots from the 36-element, 6600 in³ airgun array of the *R/V Marcus G. Langseth*. The experiment used a nested source-receiver geometry to collect data that sampled the crust and topmost mantle beneath an approximately 90-km-by-50-km area centered on the ridge segment. The segment-scale upper mantle structure was targeted with six 105-km-long lines shot at a maximum distance of 30 km from the ridge axis and two ridge-perpendicular lines shot along the northern and southern limits of the experiment. An intermediate-scale grid was comprised of 19 shot lines spaced 1 km apart within a 20-km-by-60-km region centered on the shallow central plateau. This grid recorded travel-time data for imaging off-axis structure and the along-axis distribution of the crustal magmatic plumbing system. The finest grid covered a 10-km-by-20-km area centered near the Main Endeavour vent field (47°57'N, 129°06'W) and comprised 10 shorter (20-km-long) shot lines interlaced within the crustal grid. This central grid included the densest shot and receiver distributions and was designed to image the detailed structure of the upper crust near the hydrothermal vent fields. Shot spacing along all lines was 450 m. All shot lines were obtained with the airgun array towed at 9-m depth; the middle 105-km-long, ridge-parallel lines on each flank were reshot with the airguns towed at 15-m depth to increase the low-frequency content of the source signal.

Instrument and shot locations were determined simultaneously by inverting acoustic-water-wave arrivals [Creager and Dorman, 1982] that were automatically picked using an autoregressive method [Takanami and Kitagawa, 1988]. Water column velocity structure was determined from expendable bathythermograph profiles collected throughout the experiment. The final horizontal 1- σ location uncertainties for stations and shots were 13 m and 9 m, respectively. Vertical station uncertainty was 10 m, as determined from the bathymetric map obtained using the onboard EM122 multibeam system.

The data return was remarkably high, with 62 stations recording data on either the hydrophone or vertical channel, 44 instruments yielding good quality data on both the hydrophone and vertical channels, and only 2 sites with bad data on both channels. Figure 3 shows several examples of crustal arrivals recorded by a station on the east flank of the central Endeavour (Figure 2). Ray paths that do not cross the ridge axis exhibit impulsive first-arriving (P_g) energy with a high signal-to-noise ratio and good trace-to-trace coherency at shot-receiver offsets up to 35 km (Figure 3a-b). Waveforms from P_g ray paths that propagate across the ridge

axis generally exhibit a more complex shape where first-arriving energy is emergent and attenuated (Figure 3c).

We adopted an iterative strategy for compiling a catalog of Pg travel-times. We first picked impulsive arrivals for non-ridge-crossing ray paths at small source-receiver offsets of < 10 km. We progressively increased the range of picks by inverting the data for velocity structure and using the results to generate predicted travel-times that guided subsequent picking efforts at larger ranges. For non-ridge-crossing ray paths, picking first arrivals was possible up to ranges of ~ 35 km. However, the maximum pick range was generally much smaller for ridge-crossing ray paths (~ 20 km) due to lower amplitudes and a lack of trace-to-trace coherency of waveforms. The total data set includes 96,156 Pg travel-times picked on the 62 reporting instruments. For 44 of the 62 instruments, arrival times were picked after summing the vertical and hydrophone channels while arrivals for the remaining 18 instruments were identified on one channel, depending on data quality.

Pick uncertainties were estimated visually, with larger uncertainties assigned to waveforms with an emergent first arrival, or to groups of waveforms that showed significant trace-to-trace variability. Nearly 80% of our Pg data were assigned an uncertainty between 10 and 15 ms while $\sim 97\%$ were assigned uncertainties less than 20 ms. The root-mean-square uncertainty for the entire Pg dataset is 13 ms. We note that other sources of experimental error that include source or receiver location uncertainties, instrument clock corrections and seafloor bathymetry, result in travel time uncertainties that are generally smaller than the picking error [Barclay *et al.*, 1998].

4. Tomographic Method

We used a tomographic technique to invert travel-time data for isotropic slowness and seismic anisotropy [Toomey *et al.*, 1994; Dunn *et al.*, 2005]. Assuming an initial model, we forward modeled predicted travel times and calculated residuals for ray paths between sources and receivers. The inverse problem was linearized about the model to obtain a set of equations that mapped model perturbations into travel time residuals. Additional equations with parameters set by the user determined the smoothness and *a priori* variance of the model. A least squares inversion of the overdetermined set of equations was used to update the model, and subsequent iterations were repeated until the RMS travel-time residual converged.

4.1 Forward Problem

The velocity model for ray tracing was parameterized in terms of slowness with nodes arranged in a rectangular grid aligned with the trend of the rise axis. Ray paths were calculated using the shortest-path ray tracing method [Moser, 1991]. The model included seafloor topography by vertically shearing columns of nodes [Toomey *et al.*, 1994]. On the basis of previous active source tomography experiments designed to image upper crustal structure above ~2 km depth [Barclay *et al.*, 1998; Dunn *et al.*, 2000], and on our source-receiver spacing, we chose a uniform grid spacing of 200 m for the ray tracing model.

Following Dunn *et al.* [2005], anisotropic slowness was parameterized on the slowness grid as:

$$u(r) = \frac{u_{iso}(r)}{1 + A(r)\cos[2\theta(r)] + B(r)\sin[2\theta(r)]} \quad (1)$$

where u_{iso} is the isotropic slowness, r is the position, θ is the ray path azimuth, and A and B are scale terms that control the magnitude and azimuthal orientation of the fast direction of anisotropy, which are given by $2(A^2 + B^2)^{0.5}$ and $\text{atan}(B/A)/2$, respectively. This parameterization allowed us to explicitly invert for three-dimensional variations in the orientation and percentage of seismic anisotropy.

Implicit in the parameterization of (1) is the assumption that P -wave anisotropy results from a hexagonal symmetry system. This system is appropriate for media where anisotropy results from aligned vertical cracks [Crampin, 1993], which has been widely accepted as the primary mechanism for seismic anisotropy in the upper oceanic crust [Barclay *et al.*, 1998; Dunn and Toomey, 2001; Seher *et al.*, 2010a]. In this system, P -wave velocities in the symmetry planes perpendicular to the crack plane can be expressed as a linear combination of $\cos(2\theta)$ and $\cos(4\theta)$ terms. Furthermore, we assume in (1) that liquid-filled cracks in the upper crust have an aspect ratio > 0.01 (thinner cracks would yield P -wave velocity structure that is primarily modulated by $\cos(4\theta)$ terms [Hudson, 1981]). As discussed below, this assumption is justified by the observed $\cos(2\theta)$ azimuthal variation in isotropic travel-time residuals.

4.2 Inverse Problem

Following *Toomey et al.* [1994], the inverse problem was solved using an iterative technique that required the user to set *a priori* model uncertainties and smoothing parameters that operated on perturbational models parameterized for isotropic slowness and anisotropy. The perturbational models comprised rectilinear grids that were denser within 10 km of the central axial valley to reflect the greater number of ray paths; horizontal node spacing was 1 km outside of this region and 0.5 km within. Vertical node spacing was a uniform 0.25 km. Inversions were regularized by penalizing model roughness and size. A jumping strategy was used to seek a final model that was smoothed relative to the starting model [*Shaw and Orcutt*, 1985]. We sought to minimize a functional of the general form:

$$s^2 = \Delta t' C_d^{-1} \Delta t + \lambda_p (m_0 + \Delta m)' C_m^{-1} (m_0 + \Delta m) + \lambda_v (m_0 + \Delta m)' C_v^{-1} (m_0 + \Delta m) + \lambda_H (m_0 + \Delta m)' C_H^{-1} (m_0 + \Delta m) \quad (2)$$

where Δt is a vector of the differences between observed and calculated travel times; C_d is a diagonal matrix of the data variance composed of the squares of the Pg arrival-time uncertainties; m_0 is a vector of the cumulative perturbation to the isotropic slowness and anisotropic model parameters from previous iterations; Δm is the model perturbation for the current iteration; C_m is a diagonal matrix of the *a priori* model variance; C_v and C_H are matrices that apply vertical and horizontal Gaussian smoothing, respectively, to each model parameter with a characteristic length of the Gaussian equal to the node spacing; and λ_p , λ_v and λ_H are weighting parameters. The inversion procedure also allowed separate values of the smoothing weights for isotropic slowness and anisotropic model parameters where λ_{AV} and λ_{AH} are smoothing weights for anisotropic parameters.

Because the solution to the inverse problem is inherently non-unique, our strategy was to explore the parameter space of the weighting parameters using a systematic approach to construct smooth solutions that adequately fit the data according to the function:

$$\chi^2 = \frac{1}{N} \sum_{i=1}^N \frac{\Delta t_i^2}{\sigma_i^2} \quad (3)$$

where N is the number of travel time observations and Δt_i and σ_i are the travel time residual and pick uncertainty of the i th travel time, respectively.

5.0 Results

The inversion volume (Figures 1-2) measured 90 km x 120 km x 9 km, was centered on the Endeavour segment, and was rotated clockwise 21° so that the y-axis approximately paralleled the central portion of the spreading axis. The starting model for our inversions (Figure 4a) was a smoothed approximation to a one-dimensional crustal model derived from a seismic refraction experiment conducted along the central portion of the Endeavour segment between 47°55'N and 48°05'N [Cudrak and Clowes, 1993]. We adopted a two-stage inversion approach to obtaining a preferred model that includes isotropic and anisotropic structure. First, using the one-dimensional starting model, we inverted the data for isotropic and anisotropic structure with $\lambda_P = 1$, $\lambda_V = 200$, $\lambda_H = 300$ and $\lambda_{AV} = \lambda_{AH} = 400$. A smoothed approximation to the longer wavelength isotropic structure was obtained from this inversion by applying a three-dimensional median filter to the isotropic output model using averaging half-lengths of 1 km, 5 km, and 0.6 km in the x, y, and z directions, respectively. Second, we performed a series of anisotropic inversions using the spatially smoothed isotropic starting model in which we systematically varied λ_P , λ_V , λ_H , λ_{AV} , and λ_{AH} . We assumed *a priori* model uncertainties of 50% and our preferred model does not heavily penalize the model norm ($\lambda_P = 1$), but instead penalizes vertical and horizontal roughness for both the isotropic ($\lambda_H = \lambda_V = 200$) and anisotropic components ($\lambda_{AH} = \lambda_{AV} = 400$). Varying the values of horizontal smoothing had a much larger impact on the final misfit than varying vertical smoothing. Larger values for spatial smoothing gave smoother models with lower amplitude anomalies while smaller values yielded models with higher amplitude fine-scale features. The preferred model is the smoothest model that achieved a χ^2 value reasonably close to unity (1.17).

Our strategy for testing the resolution of the preferred model involved analyzing the spatial distribution of ray paths within the experiment geometry, and conducting inversions of travel times obtained from synthetic slowness and anisotropy models. These results are presented in the Supplementary Documents.

5.1 Isotropic Structure

Average velocity-depth profiles (Figure 4a) for well resolved regions reveal large differences in upper crustal structure between the flanks of the segment center and the ends of the segment near the OSCs, including the adjacent relict Middle Valley segment (blue and red boxes, respectively, Figure 2). Upper crustal velocities in the Cobb OSC, the E-WV OSC, and

the southern end of Middle Valley are uniformly slower than our starting model, with Middle Valley displaying the lowest velocities of the three at all depths. In contrast, velocity-depth profiles near the segment center for the eastern and western flanks exhibit similar structure, both with slightly higher velocities than the starting model below 1 km depth (Figure 4a). The velocity difference between the Middle Valley region and the ridge flanks exceeds 1.0 km/s from 1.0 to 2.5 km depth.

The segment-scale velocity structure (Figure 5) is strongly heterogeneous. Beneath the E-WV OSC, we observe a broad low-velocity anomaly at all depths, with a peak velocity anomaly of -1.0 km/s. To the east of the northern Endeavour segment is another broad low-velocity anomaly that reaches -1.2 km/s and is elongated in a ridge-parallel direction. This anomaly coincides with the south end of the relic Middle Valley segment (Figure 1). At the Cobb OSC there is another broad low-velocity region. However, the peak velocity anomaly in this region (-0.7 km/s) is less than that observed within the E-WV OSC. Low velocities are also observed in the southeast corner of the model to the west of the Northern Symmetric segment in a region that coincides with a failed propagator of the Cobb OSC (Figure 1). The detailed velocity structure is only well constrained in a portion of each OSC due to the spatial limitations of ray coverage and this is reflected in the synthetic checkerboard tests (see Supplementary Documents). However, the OSCs clearly exhibit lower velocities compared to the rest of the segment. In contrast to the ends, the central portion of the Endeavour segment shows a markedly different structure with higher average velocities and substantial lateral heterogeneity (Figures 4a and 5). At depths ≥ 2.0 km, the flanks of the segment center are characterized by a broad high-velocity anomaly with peak velocity variations of 0.4 km/s that extend from a few kilometers of the spreading axis to near the eastern and western limits of the imaged region (Figures 5e-g).

Within the upper 1 km of the central portion of the Endeavour segment is a sequence of banded velocity anomalies that align with the trend of the ridge axis (Figure 6). The bands are about 4 km wide, extend 30 to 40 km along-axis and 10 km to 12 km to either side. None of the low-velocity bands locate directly beneath the bathymetric highs, but are instead displaced toward the flankward side of the ridge (Figure 7b-d). The ridge-parallel lineations are most prevalent within the upper ~ 1 km of crust, but persist as lower amplitude features to 1.6 km depth (Figure 6c-d). At depths of ≥ 2 km the ridge axis is characterized by a low velocity band flanked by high velocities. Note that since the inversions include no arrivals propagating below

the AMC the axial structure at these depths is constrained entirely by Pg phases diffracting above the AMC [Wilcock *et al.*, 1993].

Within the Endeavour axial valley there is significant along-axis heterogeneity (Figure 7e). At depths <2 km velocities beneath the hydrothermal vent fields are generally higher than elsewhere along the ridge axis. Velocities beneath the northernmost Salty Dawg and Sasquatch vent fields are up to 0.4 km/s greater than the regions immediately to the north and south of the vent fields (Figure 7e) while velocities beneath the High Rise, Main Endeavour and Mothra vent fields are up to 0.2 km/s greater than beneath the region to the south. At ~ 2.0 km depth immediately above the AMC, there are low-velocity anomalies between the Main Endeavour and High Rise vent fields and several kilometers to the north of Sasquatch field.

5.2 Anisotropic Structure

Figure 8 shows average travel time residuals in 20° azimuthal bins for a three-dimensional isotropic model plotted against the azimuth of the Y-axis of the tomography grid for three different depth intervals; the isotropic model was obtained in an identical manner to the preferred anisotropic model except that anisotropy was not included in the tomographic analysis. The travel-time residuals show a clear $\cos(2\theta)$ azimuthal variation, which is consistent with faster propagation along ray paths oriented parallel to the trend of the Endeavour segment. The peak-to-peak amplitudes of these azimuthal variations decrease from 25 ms for rays turning above 2 km depth to 9 ms for those turning between 2 and 3 km depth, indicating the azimuthal dependence is strongest at shallower depths.

The tomographic inversion recovers a substantial component of anisotropic structure, with the percentage anisotropy dependent on both the depth and distance from the ridge axis. The horizontally averaged percentage of anisotropy within 10 km of the ridge axis decreases from over 8% in the upper 1 km to just over 2% at 3 km depth (Figure 9). At all depths, the percentage of anisotropy is highest on the ridge axis and decreases substantially off-axis over a length scale of 5 to 10 km (Figure 10a-c). For example, at 1 km depth the average percentage of anisotropy decreases from $\sim 10\%$ on-axis to $\sim 4\%$ 10 km away (Figure 10b). Synthetic tests (see Supplementary Documents) show that this decrease is well resolved.

At depths between 1 and 3 km the off-axis decrease in anisotropy is accompanied by increased seismic velocities (Figure 11). At 1 km depth, the 6% decrease in anisotropy coincides

with an increase in mean velocity from 5.1 km/s to 5.4 km/s (Figure 11b). At 2.2 km depth, the percent anisotropy decreases from 5% to 3% while mean velocities increase from 6.2 km/s to 6.5 km/s (Figure 11e). Above 1 km depth, the decrease in anisotropy is not accompanied by a systematic trend in velocities (Figure 11a).

High levels of anisotropy are observed everywhere near the ridge but there is significant along-axis heterogeneity (Figure 10a-c). A checkerboard test (see Supplementary Documents) suggests that features with horizontal wavelengths as small as 10 km are resolvable in the center of the experiment; smaller wavelength features may not be resolved. The highest amplitude signal occurs to the north of the vent fields near $Y = 15$ km (Figure 10a-c). There, shallow anisotropy values exceed 15% and relatively high values persist to 2 km depth. This strongly anisotropic region is shifted slightly toward the Pacific plate and coincides with the southern extent of the E-WV OSC. Other localized zones of high anisotropy are observed near $Y = 5$ km just north of Sasquatch field, beneath the southern vent fields, and to the south near $Y = -20$ to -15 km (Figure 10a-c).

As might be expected, the overall direction of the fast axis of anisotropy parallels the central Endeavour segment but there are variations in azimuth that seem to mirror morphological features. In the E-WV OSC, the anisotropy rotates to parallel the curvature of the Endeavour arm of the OSC. Towards the south between $Y = -20$ km and $Y = -30$ km the fast direction on either side of the ridge converges to the south, mimicking the converging trends of the abyssal hills. At off-axis distances greater than ~ 10 km, where the level of the anisotropy is greatly reduced, the fast direction is variable but is less well resolved due to incomplete azimuthal ray path coverage outside of the crustal grid (see Supplementary Documents).

6. Discussion

6.1 Isotropic velocity structure

6.1.1 Segment-scale velocity variations

Our data indicate that increased fracturing in the OSCs causes low velocities in the upper crust that persist off-axis and record the history of ridge propagation. The broad zone of

relatively high velocities in the segment center is bordered by low-velocity regions that coincide closely with the regions influenced by the OSCs (Figure 5). In the southeast corner of our model, low velocities are observed to the east of the Cobb OSC in a region of a failed rift that terminated near 47°50'N (Figure 1) [Johnson *et al.*, 1983]. To the north, low velocities are observed to the east of the E-WV OSC in Middle Valley and to the west in the vicinity of the Heck Seamounts. Thus, the velocities are not uniformly low within the OSC discordant zone but appear to result from the fracturing associated with episodic events of ridge propagation.

Tomographic studies show that intra-segment variability of upper crustal velocity structure is not exclusive to the Endeavour. Figures 4b-c show average velocity profiles from this study compared to example profiles for the East Pacific Rise [Canales *et al.*, 2003] and the Mid-Atlantic Ridge [Hooft *et al.*, 2000]. The vertical velocity functions for the eastern and western flanks of the central Endeavour segment are similar to previously published results from the central Endeavour [Cudrak and Clowes, 1993; Barclay and Wilcock, 2004], and from the CoAxial Segment of the Juan de Fuca Ridge [Sohn *et al.*, 1997]. They are also quite similar to the structure observed in the center of segments along the Mid-Atlantic Ridge near 35°N (Figure 4c) [Hooft *et al.*, 2000]. At sites away from segment boundaries on the East Pacific Rise at 8-10°N (Figure 4b) [Canales *et al.*, 2003] and elsewhere [Grevemeyer *et al.*, 1998; Bazin *et al.*, 2001; Van Avendonk *et al.*, 2001] the upper crustal velocities are up to ~0.5 km/s faster than values for the central Endeavour segment. However, if the profiles from the East Pacific Rise and Endeavour are scaled relative to the depth of the AMC (~1.6 km on the northern East Pacific Rise [Detrick *et al.*, 1987; Kent *et al.*, 1993] and ~2.5 km on the Endeavour [Van Ark *et al.*, 2007]) they are quite similar. Thus, the differences may simply reflect the thinning of layer 2 units on the East Pacific Rise.

There are also strong similarities between velocity profiles at the ends the Endeavour segment and segment boundaries elsewhere. The profiles for the E-WV OSC and the relic OSC basin on the west side of the East Pacific Rise near 9°N [Canales *et al.*, 2003] are nearly identical (Figure 4b). Above 2 km, the E-WV OSC profile is also reasonably similar to the profile at the end of segment OH2 on the Mid Atlantic Ridge [Hooft *et al.*, 2000] (Figure 2c). Below 2 km, the OH2 profile is markedly faster, likely as a result of thinner crust at the end of this segment. The velocity profile for Middle Valley is similar to the Oceanographer Fracture Zone above 3 km depth [Hooft *et al.*, 2000].

Bazin et al. [2001] propose that anomalously low velocities observed in the shallow crust near the 9°N OSC on the East Pacific Rise are attributed to thickness variations caused by lavas pooling within the overlap basin. However, this model cannot explain the differences at the Endeavour. The low velocities at the segment ends extend well below 1 km, the maximum depth to which layer 2A thickness variations map into the tomographic models (see Supplementary Documents). At the northern end of the segment, where the velocities are lowest, layer 2A is thin beneath the ridge-axis [*Van Ark et al.*, 2007]. Since the West Valley segment has only been actively spreading for 10-50 kyr [*Davis and Villingner*, 1992], it seems unlikely that a thick layer of extrusive volcanic rocks could have accumulated in the E-WV OSC during this time.

Our preferred interpretation of the lower upper-crustal velocities observed at the ends of the Endeavour segment and adjacent Middle Valley is that there is increased porosity due to enhanced tectonic fracturing within the OSC. Near large transform faults, depressed seismic velocities are commonly attributed to tectonic fissuring and cracking [*Detrick et al.*, 1993a; *Begnaud et al.*, 1997; *Van Avendonk et al.*, 2001]. Within smaller overlap basins, shearing of the seafloor fabric and rotation of adjacent limbs of the overlap basin [*Christeson et al.*, 1997] can produce porosity increases of ~10%. In addition, vigorous hydrothermal circulation on the axis of the central Endeavour may decrease porosity through mineral precipitation [*Lowell et al.*, 1993], which would increase seismic velocities. In contrast, fracturing that occurs within the OSC basins may occur too far off axis to be impacted by high-temperature hydrothermal circulation so that the low velocities are preserved off-axis, recording the history of ridge propagation.

On the basis of the remarkable similarity between velocities in the E-WV OSC and the relic OSC near 9°N East Pacific Rise [*Canales et al.*, 2003] (Figure 4b), it seems plausible that fracturing may account for low velocities in this latter location. While *Bazin et al.* [2001] interpret velocity variations in terms of layer 2A thickness, the low velocity regions in their tomographic model appear to extend well below 1 km depth, which is consistent with enhanced fracturing throughout the upper crust. It is interesting to note that the average and even minimum velocities reported by *Bazin et al.* [2001] (Figure 4b) near the current OSC basin at 9°N are markedly higher than those observed by *Canales et al.* [2003] in a relict basin, which might suggest that the fracturing of the crust in the near-axis region imaged by *Bazin et al.* [2001] may not be complete.

The average velocities in the E-WV OSC are lower at all depths by 0.3 – 0.4 km/s than in the Cobb OSC (Figure 4a). This may reflect more intensive tectonic deformation associated with ongoing plate boundary reorganization at the northern end of the Endeavour segment [Dziak, 2006]. The lowest velocities in the model are in Middle Valley, where they are ~0.2 km/s slower than in the E-WV OSC (Figure 4a). Middle Valley is blanketed by a significant layer of sediment [Davis and Villinger, 1992]. The sediment layer has a low velocity and its insulating effect may also depress the velocities of the underlying basement by elevating its temperature. Ultrasonic measurements on mafic rocks suggest that the partial derivative of *P*-wave velocity with temperature is -0.4×10^{-3} to -0.6×10^{-3} km s⁻¹ K⁻¹ [Christensen, 1979; Kern and Tubia, 1993], which is equivalent to a decrease in velocities of about 0.1 – 0.2 km/s for a 300°C temperature increase.

6.1.2 Upper crustal formation

We interpret the shallow ridge-parallel, alternating velocity anomalies in the segment center as being caused by a combination of normal faults forming the rift valley and volcanic emplacement occurring in a wide zone of accretion. The upper 1 km of crust along the central axial valley and the adjacent bathymetric ridges is characterized by a series of ~4-km-wide linear anomalies that alternate between relatively high and low velocities (Figures 6 & 7). These variations are most simply interpreted in terms of variations in the thickness of layer 2A. The inversions have poor vertical resolution in the uppermost crust (see Supplementary Documents) because rays do not turn in layer 2A, so variations in the thickness of this low velocity layer are mapped into anomalies that extend throughout the upper ~1 km. The magnitudes of the shallow velocity anomalies in our isotropic model suggest variations in layer 2A thickness of 150 – 200 m, which are consistent with layer 2A thicknesses observed on cross-axis MCS profiles which have standard deviations of ~100 m [Van Ark et al., 2007].

At the Endeavour segment, periodic spacing of abyssal hills has been interpreted in terms of alternating episodes of enhanced volcanism and tectonic extension [Kappel and Ryan, 1986]. If layer 2A is interpreted as the layer of volcanic extrusives, this model predicts a variable thickness for layer 2A with thicker accumulations beneath the bathymetric ridges and less accumulation in between. Both a small tomographic experiment [Barclay and Wilcock, 2004] and MCS data [Van Ark et al., 2007] have shown a thicker layer 2A beneath bathymetric highs.

However, our results show a more nuanced structure with the low velocity anomalies centered beneath the outer flanks of the bathymetric highs (Figure 7). This observation is difficult to reconcile with a model in which the axial highs are simple volcanically constructed features.

An alternative model for the abyssal hills is that they form as a result of inward-facing normal faults that are active during diking events [Carbotte *et al.*, 2006]. This model requires no fluctuations in the rate of volcanism; instead the faults are regularly spaced across axis because new faults form only when the existing faults have rifted too far off-axis to be activated by dike-induced stresses. This model is consistent with thickening of layer 2A on the outer flanks provided some eruptions either overflow the axial valley while it is narrow and shallow [Carbotte *et al.*, 2006] or occur entirely outside the axial valley. The rotation of the footwall that would accompany normal faulting would create a sloped seafloor that would lead to eruptions flowing away from the ridge axis. Seafloor observations from the Cleft segment along the southern JdFR suggest that eruptions outside the axial valley are quite common [Stakes *et al.*, 2006] and low velocity and high attenuation anomalies observed in the crust by the Endeavour tomography experiment are consistent with off-axis volcanism [Hooft *et al.*, in review].

Another interesting feature of our shallow velocity structure is that it shows no evidence of high velocities on the spreading axis that would indicate a thinner layer 2A on-axis, which is consistent with Van Ark *et al.* [2007] who did not identify a systematic difference between the thicknesses of layer 2A on- and off-axis. In contrast, layer 2A systematically thickens by up to a factor of three off-axis along the East Pacific Rise [Toomey *et al.*, 1990; Detrick *et al.*, 1993b; Harding *et al.*, 1993] and the southern Juan de Fuca Ridge [Canales *et al.*, 2005]. Stochastic modeling of dike emplacement and lava flows [Hooft *et al.*, 1996] shows that off-axis 2A thickening can be reconstructed using a narrow zone of accretion and a bimodal distribution of lava flows consisting of short-length, small-volume flows interspersed with high-volume eruptions that flow outside the accretion zone over the axial topography. At the Endeavour, the lack of thickening of layer 2A near the ridge axis suggests that the axial lava flows presently extend over a region that is similar to the width of the accretion zone. To generate the thickening of layer 2A observed on the outer flanks of the abyssal hills, either the pattern of axial accretion is different than in the past, or eruptions occur off-axis in a region that is separated from the axial accretion zone as suggested by Hooft *et al.* [in review].

6.1.3 Vent field structure

Our data suggest that velocity differences beneath the vent fields are consistent with ongoing fracturing and mineral precipitation within the hydrothermal reaction zone. At 0 – 2 km depth, the velocities beneath the vent fields are on average 0.2 to 0.4 m/s higher than beneath the ridge axis to the north and south (Figure 7e). If the higher velocities result solely from temperature differences, then shallow temperatures would be required to be at least 300°C lower in the vent fields [Christensen, 1979]. Although hydrothermal circulation will draw cold fluids into the crust, this explanation seems unlikely since models of high Rayleigh number hydrothermal circulation suggest that much of the volume infilled by circulation is warm [Coumou *et al.*, 2008]. A more plausible explanation is that the porosity is lower beneath the vent fields due to the effects of clogging by hydrothermal precipitation and alteration [Lowell *et al.*, 1993; Wilcock and Delaney, 1996; Lowell *et al.*, 2003]. Interestingly, the lowest velocities at 0 – 2 km depth in the vent field region locate midway between the Main Endeavour and High Rise fields, the two fields with the highest heat fluxes [Kellogg, 2011]. This suggests that porosity (and, by inference, permeability) might be higher in this region.

It is also possible that increased temperatures in the heat uptake zone associated with vigorous hydrothermal circulation above the AMC may contribute to lower velocities beneath the Main Endeavour and High Rise fields (Figure 7e). The low velocities below the Main Endeavour and High Rise fields coincide closely with a region of intense seismicity (Figure 12b) whose characteristics were interpreted in terms of cracking associated with magma chamber inflation [Wilcock *et al.*, 2009]. Thus, the low velocities may reflect enhanced porosity and fracturing in a region where the high rates of seismicity counteract the effects of hydrothermal clogging. Indeed, it is interesting to note that low velocities are also present at ~2 km depth several kilometers north of the vent fields ($Y = 7$ km in Figure 12b). This is also a region of intense seismicity (Figure 12c) that may be related to stresses induced by the interaction between the southern tip of the West Valley propagator and the Endeavour segment [Weekly *et al.*, 2013].

6.2 Anisotropic crustal structure

Our study is the first to investigate the three-dimensional spatial heterogeneity of anisotropy in the upper crust at a mid-ocean ridge. Previous tomographic studies of crustal anisotropy reported on either azimuthal variations in travel time residuals calculated from an

isotropic velocity model or on the depth-dependence of the percentage anisotropy using a prescribed orientation [Barclay *et al.*, 1998; Dunn and Toomey, 2001; Barclay and Wilcock, 2004; Tong *et al.*, 2004; Dunn *et al.*, 2005]. Only one previous study [Sohn *et al.*, 1997] has reported three-dimensional variations in percent anisotropy, but that study used a fixed orientation.

6.2.1 Depth variations and cracks in the upper crust

Our results are consistent with models that attribute seismic anisotropy in the upper oceanic crust to cracks aligned parallel to the ridge axis [Stephen, 1985; Shearer and Orcutt, 1986]. The observed decrease in anisotropy with depth is attributed to pore volume reductions due to crack closures resulting from increased lithostatic pressures. A clear azimuthal dependence in travel time residuals is observed in our isotropic inversion whose amplitude decreases with ray-turning depth (Figure 8). Additionally, we image a substantial decrease in the average percent anisotropy with depth (Figure 9), suggesting that anisotropy is primarily confined to the upper volcanic units and is weak or absent in the underlying gabbro. Our results are similar to earlier tomography studies [Barclay *et al.*, 1998; Dunn and Toomey, 2001] that observed an azimuthal dependence in travel time residuals and attributed this relationship to vertical, water-filled cracks with an aspect ratio > 0.01 that align perpendicular to the spreading direction. The average level of anisotropy within 10 km of the ridge axis (Figure 9) is higher at all depths than reported by Dunn and Toomey [2001] from the East Pacific Rise but this is consistent with the amplitude of the azimuthal dependence of travel time residuals which is higher in our data set.

6.2.2 Variations off-axis

Our observed decrease in anisotropy with distance from the ridge is consistent with infilling of cracks by the precipitation of minerals in the near-axis hydrothermal system. A remarkable feature of our inversion that has not been reported from inversions elsewhere is the rapid decrease in anisotropy away from the ridge axis. Within 5 – 10 km of the ridge axis (crustal ages of 0.2 – 0.4 Ma) the percentage anisotropy in the upper crust decreases to less than half of its value at the ridge axis (Figures 10 and 11). At depths ≥ 1 km, this decrease in anisotropy is accompanied by an increase in average isotropic velocities by 0.3 – 0.4 km/s

(Figure 11). The inversions do not have good vertical resolution above 1 km since isotropic velocity anomalies at shallow depths are influenced by local variations in the thickness of the low velocity layer 2A. Thus, any increase in layer 2A isotropic velocities off-axis cannot be distinguished from changes in layer 2A thickness.

Multi-channel seismic data shows that layer 2A velocities both at the Endeavour [Nedimović *et al.*, 2008; Carbotte *et al.*, 2012] and many other locations [e.g., Grevemeyer and Bartetzko, 2004] increase quite rapidly within a few kilometers of the ridge axis before increasing more gradually well off-axis. At the Endeavour, multi-channel seismic data also shows that velocities in the upper few hundred meters of layer 2B increase off-axis by an average of 0.8 km/s within 0.5 Ma [Newman *et al.*, 2011]. The rapid evolution of layer 2A and 2B velocities is interpreted as evidence for the infilling of cracks by the precipitation of minerals in the near-axis hydrothermal system. Our results show that the evolution of layer 2B velocities extends to the base of layer 2 (the base of sheeted dike layer) and is consistent with this interpretation. Indeed, the infilling of ridge-parallel cracks is the only viable mechanism to reduce anisotropy with age. Newman *et al.* [2011] infer that crack infilling occurs in regions of hydrothermal downflow based on the distribution of layer 2B velocities in off-axis regions where the patterns of hydrothermal flow are known. This would lead to the inference that recharge associated with cooling newly formed crust extends several kilometers off-axis.

6.2.3 Along-axis variations

Along-axis variations in both the magnitude and orientation of anisotropy are consistent with tectonic processes. The orientation of the fast direction of anisotropy aligns perpendicular to the spreading direction near the segment center but is rotated near segment ends (Figure 10d). There are significant along-axis variations in the magnitude of anisotropy on the spreading axis (Figure 10a-c). The high values near $Y = 15$ km (Figures 10a-b) and $Y = 5$ km (Figure 10c) lie at the southern end of the E-WV OSC and the inferred southward propagating extension of the West Valley segment [Weekly *et al.*, 2013] and are consistent with high levels of ongoing deformation within the OSC. Within the vent fields the strongest shallow anisotropy is observed between the Main Endeavour and High-Rise fields (Figure 12a). Interestingly, this is a likely zone for intense hydrothermal recharge based on the inference that the circulation cells are

oriented along axis [McDuff *et al.*, 1994; Tolstoy *et al.*, 2008] and the observation that the hydrothermal heat fluxes are high for these two fields [Kellogg, 2011].

At the northern end of the Endeavour, the fast direction mirrors the curvature of the rotated limbs of the E-WV OSC. The curvature of adjacent limbs at OSCs towards one another is a common feature of an echelon ridge segments [Macdonald *et al.*, 1987; Macdonald *et al.*, 1991] and is consistent with crack propagation theory [Pollard and Aydin, 1984]. Near the Cobb OSC, the orientation of the fast direction converges to the south, mirroring the decreased spacing of abyssal hills that reflects decreased spreading rates in the OSC. Unlike at the 9°03'N OSC along the East Pacific Rise [Tong *et al.*, 2004], we find that the orientation of seismic anisotropy is consistent with depth and observe no rotation in anisotropy between the upper extrusive unit and the underlying dike layer.

7. Conclusions

Our tomographic study on the Endeavour segment of the JdFR provides some of the most detailed three-dimensional observations of upper crustal seismic velocity and anisotropy obtained to date over a spreading center. The segment includes both a central portion that hosts a mid-crustal axial magma chamber and vigorous hydrothermal systems, and two large overlapping spreading centers at the segment ends. The results thus provide insights into the role of magmatism, tectonism and hydrothermal circulation in constructing the oceanic crust.

Upper crustal *P*-wave velocities near the center of the Endeavour segment are, on average, ~1.0 km/s higher than near the segment ends. These variations are attributed to increased porosities at segment ends due to extensive tectonic fracturing within overlapping spreading centers and possibly the infilling of cracks by precipitation of minerals along the hydrothermally-active central portion of the segment. The upper 1.0 km of crustal velocity structure near the segment center is imprinted with a pattern of alternating velocity anomalies extending 10–12 km off-axis that are oriented parallel to the ridge axis. The low-velocity bands coincide with the outer flanks of off-axis abyssal hills. This pattern is attributed to localized thickening of the extrusives by eruptions that occur outside the axial valley and flow down the fault tilted blocks that form the abyssal hill topography.

Velocities are generally higher beneath the hydrothermal vent fields than along the spreading axis to the north and south. We interpret this as evidence of reduced porosity due to

mineral precipitation from hydrothermal circulation. Low velocities just above the AMC beneath the High Rise and Main Endeavour fields relative to other vent fields coincide with a region of intense seismicity and may reflect increased porosity and higher temperatures in the heat uptake zone beneath the most vigorous vent fields.

The percentage of seismic anisotropy decreases, on average, from over 8% in the upper 1 km of the crust to just over 2% at 3 km depth. Depth-dependent decreases in anisotropy are attributed to the closure of cracks from a combination of lithospheric overburden pressure and hydrothermal mineral precipitation. Seismic anisotropy decreases at all crustal depths away from the ridge-spreading axis within 5-10 km (0.2-0.4 Ma) and is accompanied by an increase in velocities below 1 km depth. This observation is consistent with rapid mineral infilling of cracks within layer 2B due to hydrothermal circulation near the ridge axis [Newman *et al.*, 2011].

Along-axis variations in the magnitude of seismic anisotropy are consistent with increased fracturing near the southern limit of the E-WV OSC and within a region of intense hydrothermal downflow between the Main Endeavour and High Rise vent fields. The fast direction of anisotropy is oriented ridge-parallel along the central Endeavour. This is consistent with the least compressive stress being aligned with the spreading direction. However, near the OSCs, the orientation of anisotropy reflects the tectonic fabric of the seafloor and is influenced by the interaction of stresses from adjacent limbs of the OSC.

Acknowledgements

We thank the officers and crew of the R/V *Marcus G. Langseth* as well as the OBS teams from Scripps Institution of Oceanography and Woods Hole Oceanographic Institution for their assistance in the acquisition of the seismic data. Additional assistance was provided by on-board passive acoustic technicians and marine mammal observers to ensure that data collection was accomplished in compliance with guidelines set forth by marine environmental assessments and permits. We thank Kenneth Creager, Thomas Pratt, Suzanne Carbotte, and an anonymous reviewer for thorough reviews. The experiment and analysis were supported by the NSF under grants numbered OCE-0454700 to the University of Washington and OCE-0454747 and OCE-0651123 to the University of Oregon.

References

- Barclay, A. H., and W. S. D. Wilcock (2004), Upper crustal seismic velocity structure and microearthquake depths at the Endeavour segment, Juan de Fuca Ridge, *Geochem. Geophys. Geosyst.*, 5, Q01004, doi:10.1029/2003GC000604.
- Barclay, A. H., D. R. Toomey, and S. C. Solomon (1998), Seismic structure and crustal magmatism at the Mid-Atlantic Ridge, 35°N, *J. Geophys. Res.*, 103(B8), 17827-17844, doi:10.1029/98JB01275.
- Bazin, S., A. J. Harding, G. M. Kent, J. A. Orcutt, C. H. Tong, J. W. Pye, S. C. Singh, P. J. Barton, M. C. Sinha, R. S. White, R. W. Hobbs, and H. J. A. Van Avendonk (2001), Three-dimensional shallow crustal emplacement at the 9°03'N overlapping spreading center on the East Pacific Rise: Correlations between magnetization and tomographic images, *J. Geophys. Res.*, 106(B8), 16101-16117, doi:10.1029/2001JB000371.
- Begnaud, M. L., J. S. McCain, G. A. Barth, J. A. Orcutt, and A. J. Harding (1997), Structure of the eastern Clipperton ridge-transform intersection, East Pacific Rise from three-dimensional seismic tomography, *Eos Trans. AGU*, 78(46, Suppl.), 675-675.
- Bohnenstiehl, D. R., R. P. Dziak, M. Tolstoy, C. G. Fox, and M. Fowler (2004), Temporal and spatial history of the 1999-2000 Endeavour Segment seismic series, Juan de Fuca Ridge, *Geochem. Geophys. Geosyst.*, 5(9), Q09003, doi:09010.01029/02004gc000735.
- Butterfield, D. A., R. E. McDuff, M. J. Mottl, M. D. Lilley, J. E. Lupton, and G. J. Massoth (1994), Gradients in the composition of hydrothermal fluids from the Endeavour segment vent field: Phase separation and brine loss, *J. Geophys. Res.*, 99(B5), 9561-9583, doi:10.1029/93JB03132.
- Canales, J. P., R. S. Detrick, D. R. Toomey, and W. S. D. Wilcock (2003), Segment-scale variations in the crustal structure of 150-300 kyr old fast spreading oceanic crust (East Pacific Rise, 8°15'N-10°5'N) from wide-angle seismic refraction profiles, *Geophys. J. Int.*, 152(3), 766-794, doi:10.1046/j.1365-246X.2003.01885.x.
- Canales, J. P., R. S. Detrick, S. M. Carbotte, G. M. Kent, J. B. Diebold, A. Harding, J. Babcock, M. R. Nedimovic, and E. Van Ark (2005), Upper crustal structure and axial topography at intermediate spreading ridges: Seismic constraints from the southern Juan de Fuca Ridge, *J. Geophys. Res.*, 110(B12), 23537-23555, doi:10.1029/2005jb003630.
- Carbotte, S. M., J. C. Mutter, and L. Q. Xu (1997), Contribution of volcanism and tectonism to axial and flank morphology of the southern East Pacific Rise, 17°10' - 17°40'S, from a study of layer 2A geometry, *J. Geophys. Res.*, 102(B5), 10165-10184, doi:10.1029/96JB03910.
- Carbotte, S. M., J. P. Canales, M. R. Nedimovic, H. Carton, and J. C. Mutter (2012), Recent Seismic Studies at the East Pacific Rise 8°20' - 10°10' N and Endeavour Segment: Insights into Mid-Ocean Ridge Hydrothermal and Magmatic Processes, *Oceanography*, 25(1), 100-112, doi:10.5670/oceanog.2012.08.
- Carbotte, S. M., M. R. Nedimovic, J. P. Canales, G. M. Kent, A. J. Harding, and M. Marjanovic (2008), Variable crustal structure along the Juan de Fuca Ridge: Influence of on-axis hot spots and absolute plate motions, *Geochem. Geophys. Geosyst.*, 9, Q08001, doi:10.1029/2007GC001922.
- Carbotte, S. M., R. S. Detrick, A. Harding, J. P. Canales, J. Babcock, G. Kent, E. Van Ark, M. Nedimovic, and J. Diebold (2006), Rift topography linked to magmatism at the

- intermediate spreading Juan de Fuca Ridge, *Geology*, 34(3), 209-212, doi:10.1130/G21969.1.
- Christensen, N. I. (1979), Compressional wave velocities in rocks at high temperatures and pressures, critical thermal gradients, and crustal low-velocity zones, *J. Geophys. Res.*, 84, 6849-6857, doi:10.1029/JB084iB12p06849.
- Christeson, G. L., P. R. Shaw, and J. D. Garmany (1997), Shear and compressional wave structure of the East Pacific Rise, 9°-10° N, *J. Geophys. Res.*, 102, 7821-7835, doi:10.1029/96JB03901.
- Coumou, D., T. Driesner, and C. A. Heinrich (2008), The structure and dynamics of mid-ocean ridge hydrothermal systems, *Science*, 321(5897), 1825-1828, doi:10.1126/Science.1159582.
- Crampin, S. (1993), A review of the effects of crack geometry on wave propagation through aligned cracks, *Can. J. Explor. Geophys.*, 29, 3-17.
- Creager, K. C., and L. R. M. Dorman (1982), Location of instruments on the seafloor by joint adjustment of instrument and ship positions, *J. Geophys. Res.*, 87(B10), 8379-8388, doi:10.1029/JB087iB10p08379.
- Cudrak, C. F., and R. M. Clowes (1993), Crustal structure of Endeavour Ridge Segment, Juan de Fuca Ridge, from a detailed seismic refraction survey, *J. Geophys. Res.*, 98(B4), 6329-6349, doi:10.1029/92JB02860.
- Davis, E. E., and C. R. B. Lister (1977), Heat flow measured over the Juan de Fuca Ridge: Evidence for widespread hydrothermal circulation in a highly heat transportive crust, *J. Geophys. Res.*, 82, 4845-4860, doi:10.1029/JB082i030p04845.
- Davis, E. E., and J. L. Karsten (1986), On the cause of asymmetric distribution of seamounts about the Juan de Fuca ridge: Ridge crest migration over a heterogeneous asthenosphere, *Earth Planet. Sci. Lett.*, 79, 385-396, doi:10.1016/0012-821X(86)90194-9.
- Davis, E. E., and H. Villinger (1992), Tectonic and Thermal Structure of the Middle Valley Sedimented Rift, Northern Juan de Fuca Ridge, *Proceedings of the Ocean Drilling Program, Initial Report*, 139, 9-41.
- Davis, E. E., K. Wang, R. E. Thomson, K. Becker, and J. F. Cassidy (2001), An episode of seafloor spreading and associated plate deformation inferred from crustal fluid pressure transients, *J. Geophys. Res.*, 106(B10), 21953-21963, doi:10.1029/2000JB000040.
- DeMets, C., R. G. Gordon, and D. F. Argus (2010), Geologically current plate motions, *Geophys. J. Int.*, 181(1), 1-80, doi:10.1111/J.1365-246x.2009.04491.X.
- Detrick, R. S., R. S. White, and G. M. Purdy (1993a), Crustal Structure of North-Atlantic Fracture-Zones, *Rev. Geophys.*, 31(4), 439-458, doi:10.1029/93rg01952.
- Detrick, R. S., A. J. Harding, G. M. Kent, J. A. Orcutt, J. C. Mutter, and P. Buhl (1993b), Seismic Structure of the Southern East Pacific Rise, *Science*, 259(5094), 499-503, doi:10.1126/Science.259.5094.499.
- Detrick, R. S., P. Buhl, E. Vera, J. Mutter, J. Orcutt, J. Madsen, and T. Brocher (1987), Multichannel seismic imaging of a crustal magma chamber along the East Pacific Rise, *Nature*, 326(6108), 35-41, doi:10.1038/326035a0.
- Dunn, R. A., and D. R. Toomey (2001), Crack-induced seismic anisotropy in the oceanic crust across the East Pacific Rise (9° 30'N), *Earth Planet. Sci. Lett.*, 189(1-2), 9-17, doi:10.1016/S0012-821X(01)00353-3.

- Dunn, R. A., D. R. Toomey, and S. C. Solomon (2000), Three-dimensional seismic structure and physical properties of the crust and shallow mantle beneath the East Pacific Rise at 9°30'N, *J. Geophys. Res.*, *105*(B10), 23537-23555, doi:10.1029/2000JB900210.
- Dunn, R. A., V. Lekic, R. S. Detrick, and D. R. Toomey (2005), Three-dimensional seismic structure of the Mid-Atlantic Ridge (35°N): Evidence for focused melt supply and lower crustal dike injection, *J. Geophys. Res.*, *110*(B9), doi:10.1029/2004JB003473.
- Durant, D. T., and D. R. Toomey (2009), Evidence and implications of crustal magmatism on the flanks of the East Pacific Rise, *Earth Planet. Sci. Lett.*, *287*(1-2), 130-136, doi:10.1016/j.epsl.2009.08.003.
- Dziak, R. P. (2006), Explorer deformation zone: Evidence of a large shear zone and reorganization of the Pacific-Juan de Fuca-North American triple junction, *Geology*, *34*(3), doi:10.1130/g22164.22161.
- Grevemeyer, I., and A. Bartetzko (2004), *Hydrothermal aging of oceanic crust; inferences from seismic refraction and borehole studies*, Cambridge University Press, Cambridge, United Kingdom.
- Grevemeyer, I., W. Weigel, and C. Jennrich (1998), Structure and ageing of oceanic crust at 14°S on the East Pacific Rise, *Geophys. J. Int.*, *135*(2), 573-584, doi:10.1046/j.1365-246X.1998.00673.x.
- Harding, A. J., G. M. Kent, and J. A. Orcutt (1993), A Multichannel Seismic Investigation of Upper Crustal Structure at 9°N on the East Pacific Rise - Implications for Crustal Accretion, *J. Geophys. Res.*, *98*(B8), 13925-13944, doi:10.1029/93jb00886.
- Hey, R. N., and D. S. Wilson (1982), Propagating Rift Explanation for the Tectonic Evolution of the Northeast Pacific - the Pseudo-Movie, *Earth Planet. Sci. Lett.*, *58*(2), 167-188, doi:10.1016/0012-821x(82)90192-3.
- Hooft, E. E. E., H. Schouten, and R. S. Detrick (1996), Constraining crustal emplacement processes from the variation in seismic layer 2A thickness at the East Pacific Rise, *Earth Planet. Sci. Lett.*, *142*(3-4), 289-309, doi:10.1016/0012-821x(96)00101-x.
- Hooft, E. E. E., R. S. Detrick, and G. M. Kent (1997), Seismic structure and indicators of magma budget along the Southern East Pacific Rise, *J. Geophys. Res.*, *102*, 27319-27340.
- Hooft, E. E. E., R. S. Detrick, D. R. Toomey, J. A. Collins, and J. Lin (2000), Crustal thickness and structure along three contrasting spreading segments of the Mid-Atlantic Ridge, 33.5°-35°N, *J. Geophys. Res.*, *105*(B4), 8205-8226, doi:10.1029/1999JB900442.
- Hooft, E. E. E., H. Patel, W. Wilcock, K. Becker, D. Butterfield, E. Davis, R. Dziak, K. Inderbitzen, M. Lilley, P. McGill, D. Toomey, and D. Stakes (2010), A seismic swarm and regional hydrothermal and hydrologic perturbations: The northern Endeavour segment, February 2005, *Geochem. Geophys. Geosyst.*, *11*(12), Q12015, doi:10.1029/2010GC003264.
- Hudson, J. A. (1981), Wave speeds and attenuation of elastic waves in material containing cracks, *Geophys. J. R. Astr. Soc.*, *64*, 133-150, doi:10.1111/j.1365-246X.1981.tb02662.x.
- Hussenoeder, S. A., J. A. Collins, G. M. Kent, R. S. Detrick, A. J. Harding, J. A. Orcutt, J. C. Mutter, and P. Buhl (1996), Seismic analysis of the axial magma chamber reflector along the southern East Pacific Rise from conventional reflection profiling, *J. Geophys. Res.*, *101*(B10), 22087-22105, doi:10.1029/96JB01907.
- Johnson, H. P., J. L. Karsten, J. R. Delaney, E. E. Davis, R. G. Currie, and R. L. Chase (1983), A detailed study of the Cobb Offset on the Juan de Fuca Ridge: Evolution of the propagating rift, *J. Geophys. Res.*, *88*, 2297-2315, doi:10.1029/JB088iB03p02297.

- Johnson, H. P., M. Hutnak, R. P. Dziak, C. G. Fox, I. Urcuyo, J. P. Cowen, J. Nabalek, and C. Fisher (2000), Earthquake-induced changes in a hydrothermal system on the Juan de Fuca Ridge mid-ocean ridge, *Nature*, *407*, 174-177, doi:10.1038/35025040.
- Kappel, E. S., and W. B. F. Ryan (1986), Volcanic episodicity and a non-steady state rift valley along Northeast Pacific spreading centers: Evidence from Sea MARC I, *J. Geophys. Res.*, *91*, 13925-13940, doi:10.1029/JB091iB14p13925.
- Kappus, M. E., A. J. Harding, and J. A. Orcutt (1995), A baseline for upper crustal velocity variations along the East Pacific Rise at 13°N, *J. Geophys. Res.*, *100*, 6143-6161, doi:10.1029/94JB02474.
- Karsten, J. L., and J. R. Delaney (1989), Hot spot-ridge crest convergence in the Northeast Pacific, *J. Geophys. Res.*, *94*(B1), 700-712, doi:10.1029/JB094iB01p00700.
- Kelley, D. S., J. A. Baross, and J. R. Delaney (2002), Volcanoes, fluids, and life at mid-ocean ridge spreading centers, *Ann. Rev. Earth Planet. Sci.*, *30*, 385-491, doi:10.1146/annurev.earth.30.091201.141331.
- Kelley, D. S., S. M. Carbotte, D. W. Caress, D. A. Clague, J. R. Delaney, J. B. Gill, H. Hadaway, J. F. Holden, E. E. E. Hooft, J. P. Kellogg, M. D. Lilley, M. Stoermer, D. Toomey, R. Weekly, and W. S. D. Wilcock (2012), Endeavour Segment of the Juan de Fuca Ridge: One of the most remarkable places on Earth, *Oceanography*, *25*(1), 44-61, doi:10.5670/oceanog.2012.03.
- Kellogg, J. P. (2011), Temporal and spatial variability of hydrothermal fluxes within a mid-ocean ridge segment, *PhD thesis*, University of Washington, Seattle.
- Kent, G. M., A. J. Harding, and J. A. Orcutt (1990), Evidence for a Smaller Magma Chamber beneath the East Pacific Rise at 9-Degrees-30' N, *Nature*, *344*(6267), 650-653, doi:10.1038/344650a0.
- Kent, G. M., A. J. Harding, and J. A. Orcutt (1993), Distribution of Magma beneath the East Pacific Rise between the Clipperton Transform and the 9°17' N Deval from Forward Modeling of Common Depth Point Data, *J. Geophys. Res.*, *98*(B8), 13945-13969, doi:10.1029/93jb00705.
- Kent, G. M., A. J. Harding, J. A. Orcutt, R. S. Detrick, J. C. Mutter, and P. Buhl (1994), Uniform accretion of oceanic crust south of the Garrett transform at 14°15' S on the East Pacific Rise, *J. Geophys. Res.*, *99*, 9097-9116, doi:10.1029/93JB02872.
- Kern, H., and J. M. Tubia (1993), Pressure and Temperature-Dependence of P-Wave and S-Wave Velocities, Seismic Anisotropy and Density of Sheared Rocks from the Sierra Alpujata Massif (Ronda Peridotites, Southern Spain), *Earth Planet. Sci. Lett.*, *119*(1-2), 191-205, doi:10.1016/0012-821x(93)90016-3.
- Lilley, M. D., D. A. Butterfield, J. E. Lupton, and E. J. Olson (2003), Magmatic events can produce rapid changes in hydrothermal vent chemistry, *Nature*, *422*, 878-881, doi:10.1038/nature01569.
- Lowell, R. P., P. Van Cappellen, and L. N. Germanovich (1993), Silica precipitation in fractures and the evolution of permeability in hydrothermal upflow zones, *Science*, *260*, 192-194, doi:10.1126/science.260.5105.192.
- Lowell, R. P., Y. Yao, and L. N. Germanovich (2003), Anhydrite precipitation and the relationship between focused and diffuse flow in seafloor hydrothermal systems, *J. Geophys. Res.*, *108*(B9), doi:10.1029/2002jb002371.
- Macdonald, K. C., D. S. Scheirer, and S. M. Carbotte (1991), Mid-ocean ridges: Discontinuities, segments and giant cracks, *Science*, *253*, 986-994, doi:10.1126/science.253.5023.986.

- Macdonald, K. C., J. C. Sempere, P. J. Fox, and R. Tyce (1987), Tectonic Evolution of Ridge-Axis Discontinuities by the Meeting, Linking, or Self-Decapitation of Neighboring Ridge Segments, *Geology*, *15*(11), 993-997, doi:10.1130/0091-7613(1987)15.
- Magde, L. S., A. H. Barclay, D. R. Toomey, R. S. Detrick, and J. A. Collins (2000), Crustal magma plumbing within a segment of the Mid-Atlantic Ridge, 35°N, *Earth Planet. Sci. Lett.*, *175*, 55-67, doi:10.1016/S0012-821X(99)00281-2.
- McClain, J. S., M. L. Begnaud, M. A. Wright, J. Fondrk, and G. K. Von Damm (1993), Seismicity and tremor in a submarine hydrothermal field: The northern Juan de Fuca Ridge, *Geophys. Res. Lett.*, *20*(17), 1883-1886, doi:10.1029/93GL01872.
- McDuff, R. E., J. R. Delaney, M. D. Lilley, and D. A. Butterfield (1994), Are up flow zones boundaries between adjacent hydrothermal systems? (Abstract), *Eos Trans. AGU*, *75*, Fall Meeting Suppl., 618.
- Moser, T. J. (1991), Shortest path calculation of seismic rays, *Geophysics*, *56*, 59-67, doi:10.1190/1.1442958.
- Nedimovic, M. R., S. M. Carbotte, J. B. Diebold, A. J. Harding, J. P. Canales, and G. M. Kent (2008), Upper crustal evolution across the Juan de Fuca ridge flanks, *Geochem. Geophys. Geosyst.*, *9*, Q09006, doi:10.1029/2008gc002085.
- Newman, K. R., M. R. Nedimovic, J. P. Canales, and S. M. Carbotte (2011), Evolution of seismic layer 2B across the Juan de Fuca Ridge from hydrophone streamer 2-D travelttime tomography, *Geochem. Geophys. Geosyst.*, *12*, Q05009, doi:10.1029/2010gc003462.
- Pollard, D. D., and A. Aydin (1984), Propagation and linkage of oceanic ridge segments, *J. Geophys. Res.*, *89*(B12), 17-28, doi:10.1029/JB089iB12p10017.
- Seher, T., S. C. Singh, W. C. Crawford, and J. Escartin (2010a), Upper crustal velocity structure beneath the central Lucky Strike Segment from seismic refraction measurements, *Geochem. Geophys. Geosyst.*, *11*, Q05001, doi:10.1029/2009gc002894.
- Seher, T., W. C. Crawford, S. C. Singh, M. Cannat, V. Combier, and D. Dusunur (2010b), Crustal velocity structure of the Lucky Strike segment of the Mid-Atlantic Ridge at 37 degrees N from seismic refraction measurements, *J. Geophys. Res.*, *115*, B03103, doi:10.1029/2009jb006650.
- Seyfried, W. E., Jr., J. S. Seewald, M. E. Berndt, K. Ding, and D. I. Foustoukos (2003), Chemistry of hydrothermal vent fluids from the Main Endeavour Field, northern Juan de Fuca Ridge: Geochemical controls in the aftermath of the June 1999 seismic events, *J. Geophys. Res.*, *108*(B9), 2429, doi:10.1029/2002JB001957.
- Shaw, P. R., and J. A. Orcutt (1985), Waveform inversion of seismic refraction data and applications to young Pacific crust, *Geophys. J. R. Astr. Soc.*, *82*, 375-414, doi:10.1111/j.1365-246X.1985.tb05143.x.
- Shearer, P. M., and J. A. Orcutt (1986), Compressional and shear wave anisotropy in the oceanic lithosphere- the Ngendei seismic refraction experiment, *Geophys. J. R. Astron. Soc.*, *87*, 967-1003, doi:10.1111/j.1365-246X.1986.tb01979.x.
- Shoberg, T., S. Stein, and J. Karsten (1991), Constraints on rift propagation history at the Cobb Offset, Juan de Fuca Ridge, from numerical modeling of tectonic fabric, *Tectonophys.*, *197*, 295-308, doi:10.1016/0040-1951(91)90047-V.
- Singh, S. C., G. M. Kent, J. S. Collier, A. J. Harding, and J. A. Orcutt (1998), Melt to mush variations in crustal magma properties along the ridge crest at the southern East Pacific Rise, *Nature*, *394*(6696), 874-878, doi:10.1038/29740.

- Sohn, R. A., S. C. Webb, J. A. Hildebrand, and B. D. Cornuelle (1997), Three-dimensional tomographic velocity structure of upper crust, CoAxial segment, Juan de Fuca Ridge: Implications for on-axis evolution and hydrothermal circulation, *J. Geophys. Res.*, *102*, 17679-17695, doi:10.1029/97JB00592.
- Stakes, D. S., M. R. Perfit, M. A. Tivey, D. W. Caress, T. M. Ramirez, and N. Maher (2006), The Cleft revealed: Geologic, magnetic, and morphologic evidence for construction of upper oceanic crust along the southern Juan de Fuca Ridge, *Geochem. Geophys. Geosyst.*, *7*, Q04003, doi:10.1029/2005gc001038.
- Stephen, R. A. (1985), Seismic anisotropy in the upper oceanic crust, *J. Geophys. Res.*, *90*, 11383-11396, doi:10.1029/JB090iB13p11383.
- Takanami, T., and G. Kitagawa (1988), A new efficient procedure for the estimation of onset times of seismic-waves, *J. Phys. Earth*, *36*(6), 267-290, doi:10.4294/jpe1952.36.267.
- Tolstoy, M., F. Waldhauser, D. R. Bohnenstiehl, R. T. Weekly, and W. Y. Kim (2008), Seismic identification of along-axis hydrothermal flow on the East Pacific Rise, *Nature*, *451*(7175), doi:10.1038/Nature06424, doi:10.1038/nature06424.
- Tong, C. H., R. S. White, M. R. Warner, and A. W. Grp (2004), Effects of tectonism and magmatism on crack structure in oceanic crust: A seismic anisotropy study, *Geology*, *32*(1), 25-28, doi:10.1130/G19962.1.
- Toomey, D. R., S. C. Solomon, and G. M. Purdy (1994), Tomographic imaging of the shallow crustal structure of the East Pacific Rise at 9°30'N, *J. Geophys. Res.*, *99*(B12), 24135-24157, doi:10.1029/94JB01942.
- Toomey, D. R., G. M. Purdy, S. C. Solomon, and W. S. D. Wilcock (1990), The three-dimensional seismic velocity structure of the East Pacific Rise near latitude 9°30' N, *Nature*, *347*(6294), 639-645, doi:10.1038/347639a0.
- Van Ark, E. M., R. S. Detrick, J. P. Canales, S. M. Carbotte, A. J. Harding, G. M. Kent, M. R. Nedimovic, W. S. D. Wilcock, J. B. Diebold, and J. M. Babcock (2007), Seismic structure of the Endeavour Segment, Juan de Fuca Ridge: Correlations with seismicity and hydrothermal activity, *J. Geophys. Res.*, *112*(B2), B02401, doi:10.1029/2005jb004210.
- Van Avendonk, H. J. A., A. J. Harding, J. A. Orcutt, and J. S. McClain (2001), Contrast in crustal structure across the Clipperton transform fault from travel time tomography, *J. Geophys. Res.*, *106*, 10961-10981, doi:10.1029/2000JB900459.
- Weekly, R. T., W. S. D. Wilcock, E. E. E. Hooft, P. R. McGill, and D. S. Stakes (2013), Termination of a 6 year ridge-spreading event observed using a seafloor seismic network on the Endeavour Segment, Juan de Fuca Ridge, *Geochem. Geophys. Geosyst.*, *14*, doi:10.1002/2012GC004249.
- Wilcock, W. S. D., and J. R. Delaney (1996), Mid-ocean ridge sulfide deposits: Evidence for heat extraction from magma chambers or cracking fronts?, *Earth Planet. Sci. Lett.*, *145*, 49-64, doi:10.1016/S0012-821X(96)00195-1.
- Wilcock, W. S. D., S. D. Archer, and G. M. Purdy (2002), Microearthquakes on the Endeavour segment of the Juan de Fuca Ridge, *J. Geophys. Res.*, *107*(B12), 2336, doi:10.1029/2001JB000505.
- Wilcock, W. S. D., M. E. Dougherty, S. C. Solomon, G. M. Purdy, and D. R. Toomey (1993), Seismic propagation across the East Pacific Rise: Finite-difference experiments and implications for seismic tomography, *J. Geophys. Res.*, *98*(B11), 19913-19932.

Accepted Article

Wilcock, W. S. D., E. E. E. Hooft, D. R. Toomey, P. R. McGill, A. H. Barclay, D. S. Stakes, and T. M. Ramirez (2009), The role of magma injection in localizing black smoker activity, *Nature Geosciences*, doi:10.1038/NGEO1550.

Figure Captions

- 1) Bathymetric map of the Endeavour segment showing the primary tectonic and volcanic features (labeled), the traces of the Northern Symmetric, Endeavour and West Valley segments and the failed Middle Valley segment (bold black lines), an elevated region centered on the central portion of the Endeavour Ridge (shaded box), the outline of the inversion area for the tomography experiment (black dashed box) and the coordinate system for the area shown in Figure 5 (white grid). The grid of white lines are spaced 20 and 25 km apart in the x and y directions, respectively.
- 2) Configuration of the tomography experiment showing the location of over 5,500 shots from the 36-element airgun array of the *R/V Marcus G. Langseth* (black dots) and 64 sites at which OBSs from the U.S. Ocean Bottom Seismograph Instrument Pool were deployed (circles and triangles denote instruments operated by Scripps Institution of Oceanography and Woods Hole Oceanographic Institution, respectively). Three bold black lines and a filled black triangle show shots and an OBS, respectively, for the record sections displayed in Figure 3. Filled white symbols represent stations with Pg picked on the summed signal of the vertical and hydrophone channels, while filled gray symbols indicate stations where Pg was picked on a single channel. Open symbols indicate stations where no data was recorded. Rectangles show locations of averaged vertical velocity profiles displayed in Figure 4 for the flanks of the central Endeavour (blue) and the segment ends (red). The bold black dashed line shows the outline of the inversion area also shown in Figure 1.
- 3) Example record sections with Pg travel time picks (red lines with dotted lines showing assigned picking errors) used for tomographic inversions. Waveform data recorded from the shot lines shown in Figure 2 are bandpass filtered between 4 and 30 Hz and a reduction velocity of 6 km/s is applied. The shots are spaced uniformly 450 m apart along the shot lines and the horizontal axis is labeled with the shot-receiver range. (a-b) For non-ridge-crossing lines, the most impulsive arrivals are observed at ranges less than 12 km (a) but picks can often be obtained to ranges exceeding 30 km (b). (c) Ridge-

crossing lines show more complicated arrivals with lower signal to noise, particularly beyond 15 km, and are typically picked to shorter ranges and with higher uncertainties.

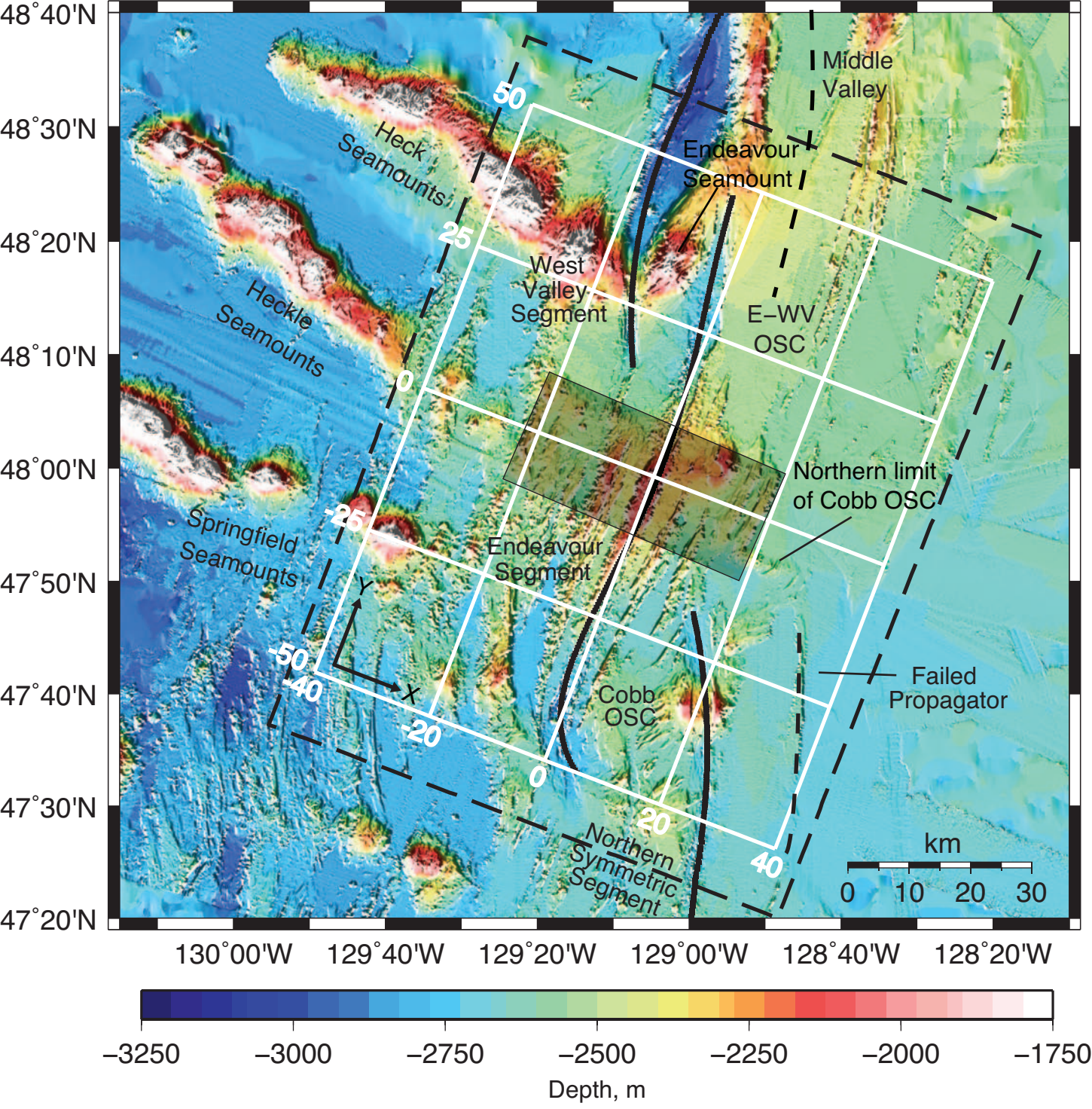
- 4) (a) The starting one-dimensional velocity model for our inversions (black dashed), derived from *Cudrak and Clowes* [1993], the horizontal average of our preferred isotropic model used to plot anomalies (black solid), and vertical profiles for the flanks of the central Endeavour (blue) and for the overlapping spreading centers and southern end of Middle Valley (red) obtained from horizontal averaging of velocities within 5-km-by-10 km regions shown by boxes in Figure 2. (b) Comparison of velocity profiles from this study with example velocity profiles obtained from 8°-10°N on the East Pacific Rise (labeled EPR in the legend) *Canales et al.* [2003] shown in green and *Bazin et al.* [2001] shown in magenta. Profiles from *Canales et al.* [2003] are for the west flank near 9°10'N in the wake of the 9°03'N OSC and for the east flank near 9°50'N away from segment boundaries. Profiles from *Bazin et al.* [2001] represent the average (dashed-dot) and minimum (dashed) velocity profiles of the study region. (c) Comparison of velocity profiles from this study with example profiles obtained from three segments lying between the Oceanographer and Hayes Fracture Zones (33°30'N – 35°30'N) on the Mid-Atlantic Ridge [*Hooft et al.*, 2000] (green). Profiles from *Hooft et al.* [2000] are from the center of the OH1 segment, the northern end of the OH2 segment and just south of the Oceanographer Fracture Zone (labeled OFZ in the legend).
- 5) (a-g) Map view sections of three-dimensional segment-scale isotropic velocity anomalies relative to the horizontally-averaged model (black solid line in Figure 4a). The area covered by the plots is shown by a dotted line in Figure 1. Horizontal slices of the inversion volume are presented at 0.4 km depth intervals and masked in regions where the derivative weight sum (DWS) is less than 10 (see Supplementary Documents). The contour interval for velocity perturbations is 0.2 km/s. The traces of the segments are shown by bold black lines and the vent fields by green stars. (h) Shaded bathymetric map of the area shown in a-g showing the location of high-temperature vent fields (green stars). Red and blue boxes show regions used for calculating the average vertical

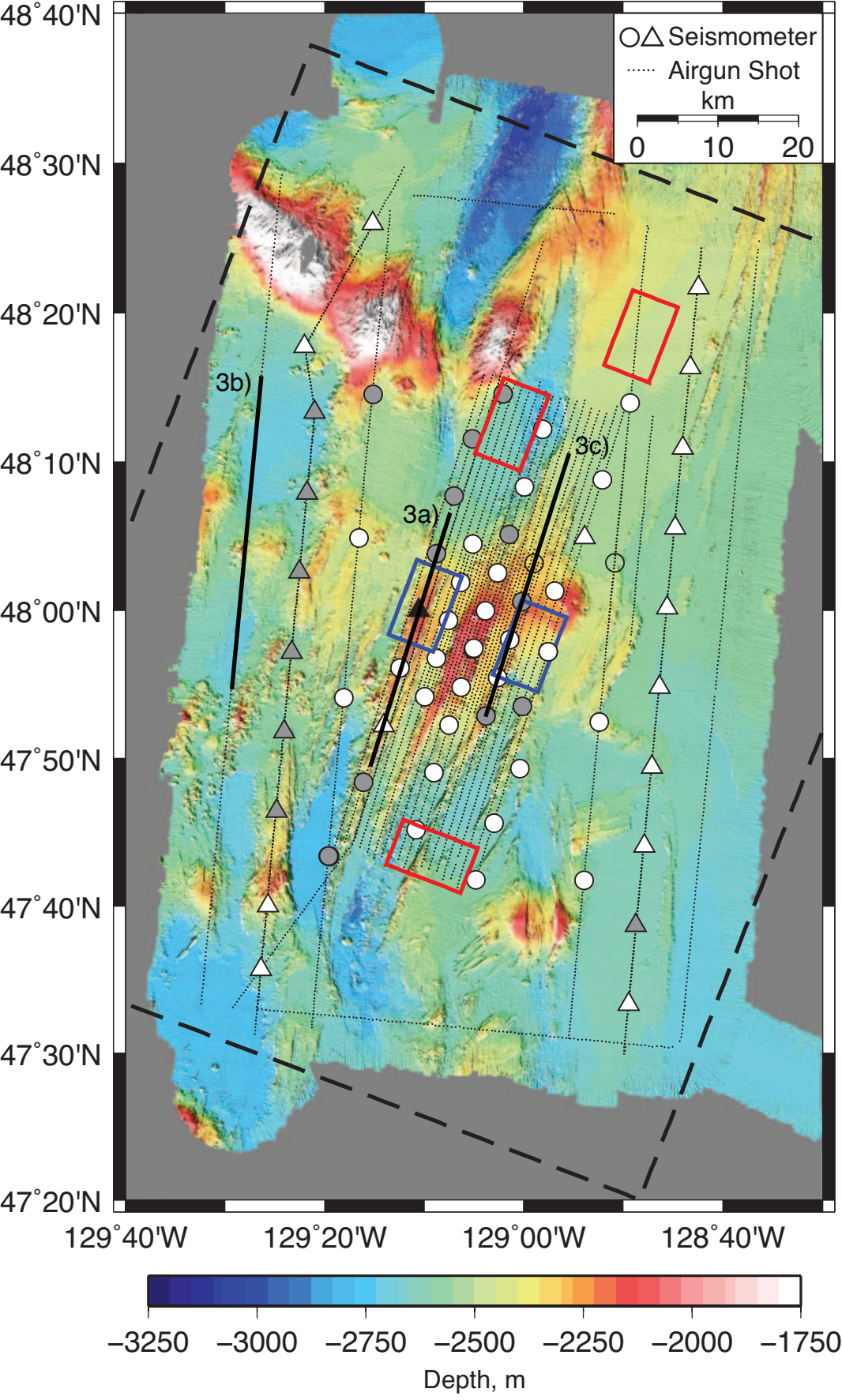
velocity profiles in Figure 4a and the black dashed box shows the area covered by Figure 6.

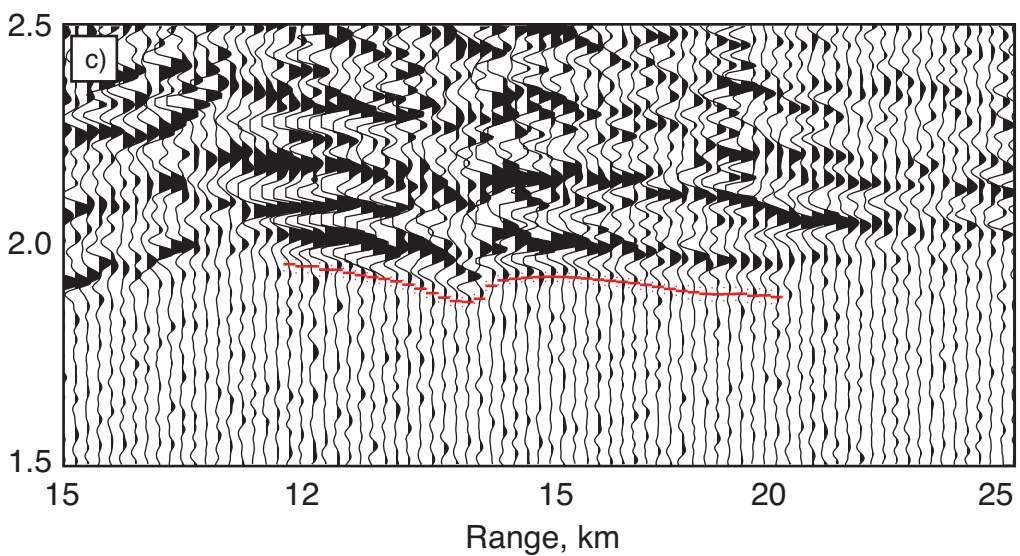
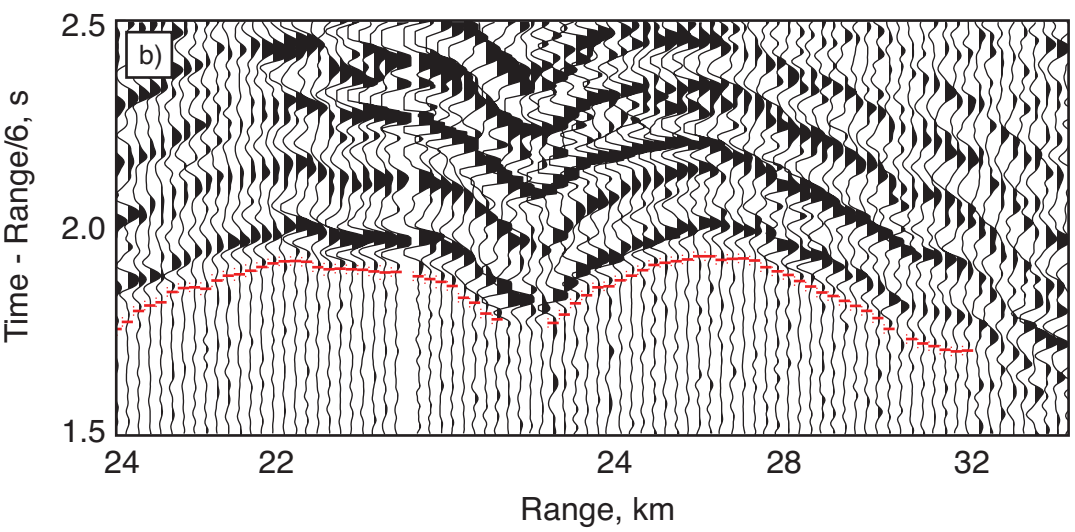
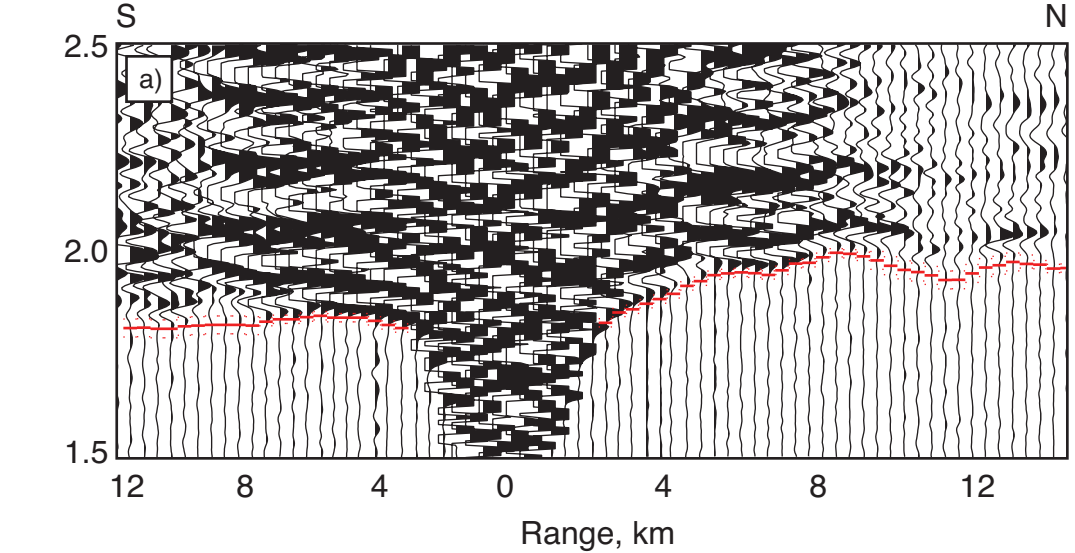
- 6) Velocity anomalies and bathymetry within the central portion of the Endeavour segment plotted with the same conventions as in Figure 5.
- 7) Vertical sections showing velocity anomalies for the central portion of the Endeavour. (a) Bathymetric map showing the locations of the vertical sections (dashed lines) and vent fields (labeled green stars). (b-d) Vertical sections crossing the ridge-axis at (b) $Y = -6$ km near the Mothra field, (c) $Y = -2$ km near the High Rise field, and (d) $Y = 2$ km near the Sasquatch field. (e) Vertical section along the ridge-axis showing vent fields (green stars) and the position of the top of the AMC (black solid line) obtained by converting two-way travel times to the AMC [*Van Ark et al.*, 2007] to depth assuming the horizontally averaged velocity model from the inversion.
- 8) Mean travel time residuals for the preferred isotropic model plotted against azimuth for rays turning between (a) 0 – 1 km depth, (b) 1 – 2 km depth, and (c) 2 – 3 km depth. Residuals are averaged in 20° azimuth bins and error bars show the $1-\sigma$ standard error of the mean. Azimuths are plotted as degrees clockwise from the y-axis of the inversion grid, which is parallel to the strike of the central Endeavour and rotated 21° clockwise from north. Solid lines depict cosine curves of the form $a \cos(2\theta + b)$ that have been fit to the data using a least-squares approach.
- 9) Average vertical profile of percent anisotropy recovered by the inversion within $X = -10$ and 10 km of the ridge-axis and between $Y = -20$ km and $Y = 20$ km.
- 10) Map-view sections of the central Endeavour showing the magnitude of anisotropy at (a) 0.4 km depth, (b) 1.0 km depth, and (c) 1.6 km depth. Images are contoured at 2% intervals. (d) Map of the central Endeavour segment showing orientation and magnitude of seismic anisotropy at 0.4 km depth with ticks showing the fast direction and tick

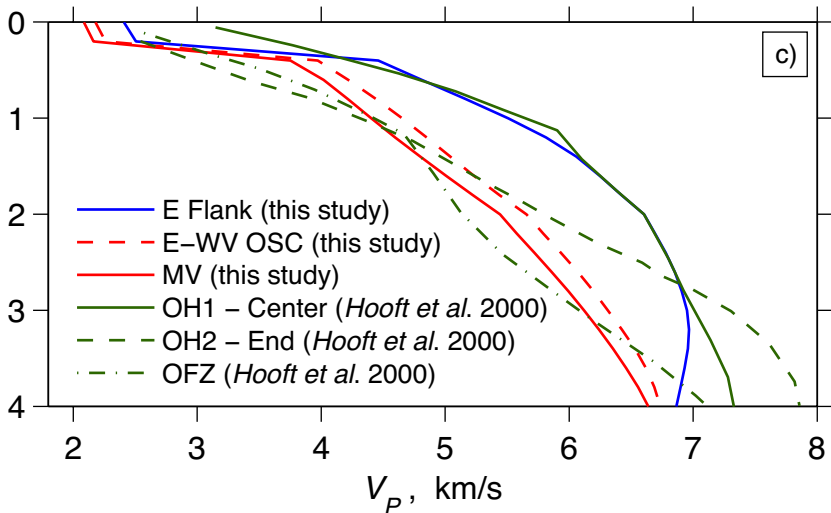
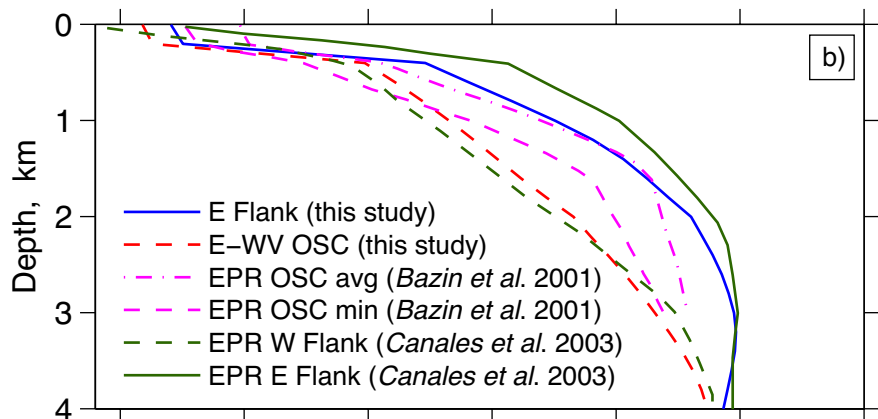
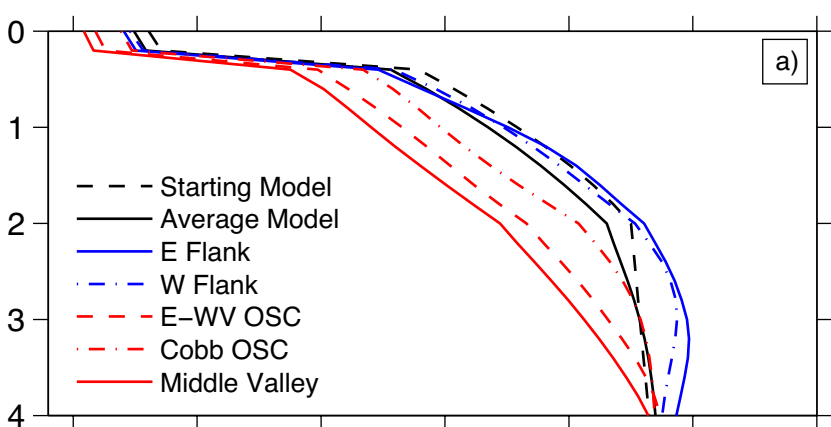
lengths scaled to the magnitude of anisotropy. The traces of segments (bold cyan lines in a-c and black lines in d) and vent fields (green stars) are also shown.

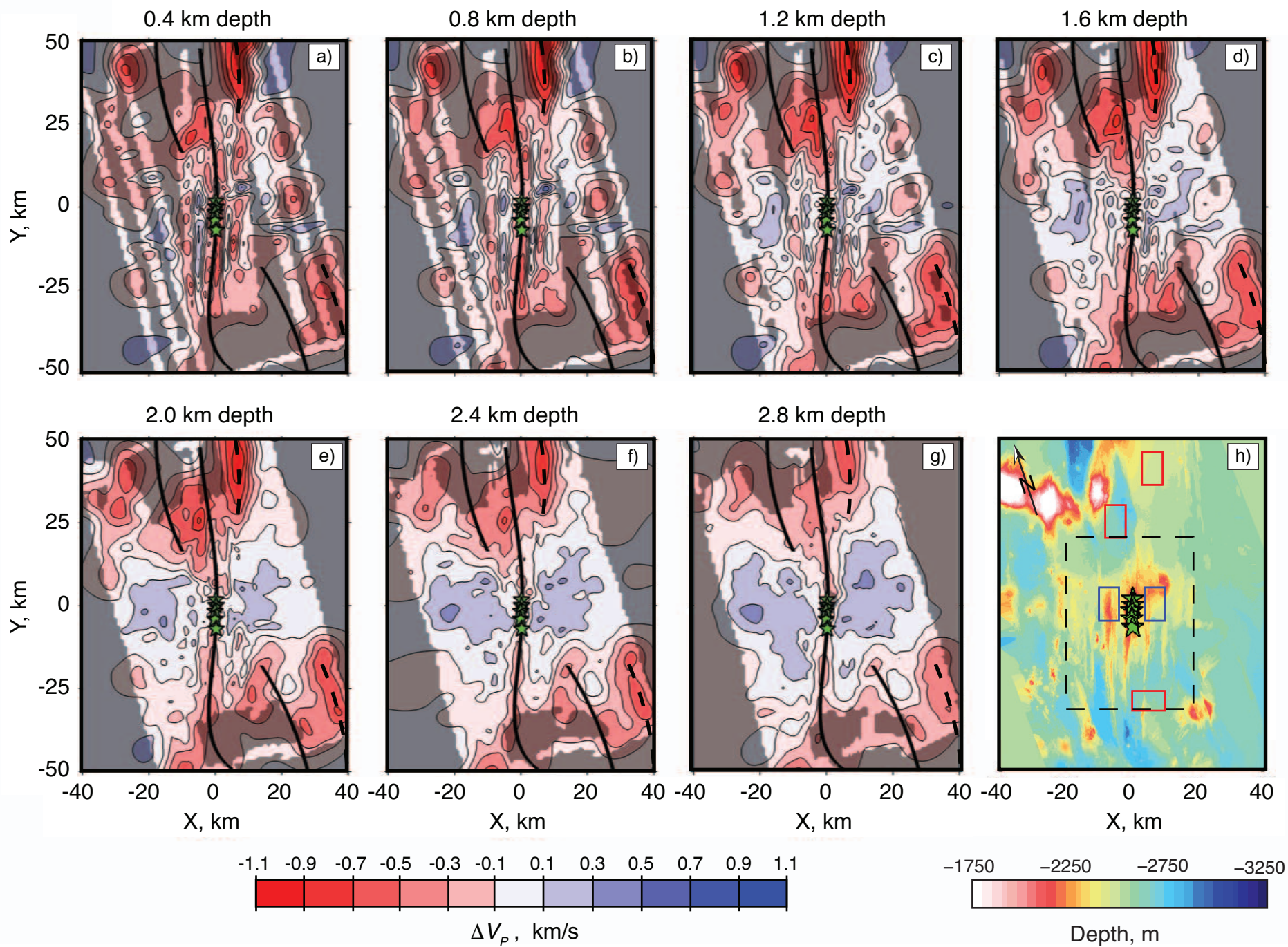
- 11) Plots showing the change in average isotropic velocity (blue lines) and magnitude of anisotropy (red lines) as a function of distance from the ridge-axis of the central Endeavour at six depths (labeled). Average values at depth were calculated in 1-km-wide and 40-km-long bins oriented parallel to the Y-axis and bisected by the X-axis.
- 12) (a) Along-axis ($X = 0$ km) vertical cross-section showing the percentage anisotropy for the region extending from $Y = -10$ to $Y = 10$ km. Locations of earthquakes between 2003 and 2004 (red dots) were obtained using double-difference techniques [Wilcock *et al.*, 2009]. The black solid line shows the depth to the AMC [Van Ark *et al.*, 2007]. (b) As for (a), but showing the magnitude of isotropic velocity anomalies for our preferred model plotted relative to the average velocity structure shown in Figure 4a. (c) Histogram of ~6,000 earthquakes located by an automated method from 2003 – 2006 that occurred within 2 km of the ridge [Weekly *et al.*, 2013]. Earthquakes are binned in 0.5 km increments along the Y-axis. Hypocenters from this dataset are not shown because earthquakes located north of the vent fields occurred outside of the seismometer network and have poor depth constraints.

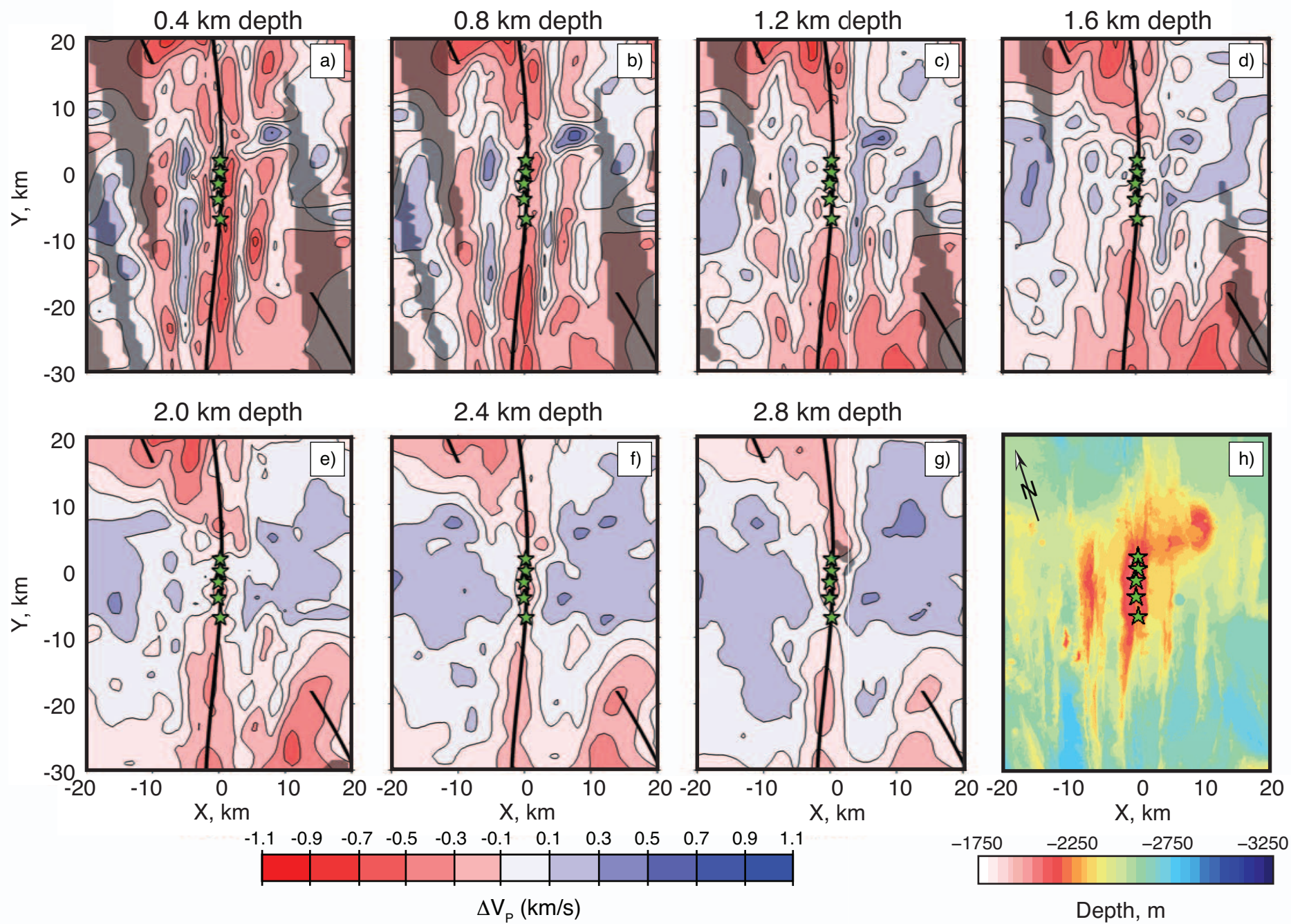


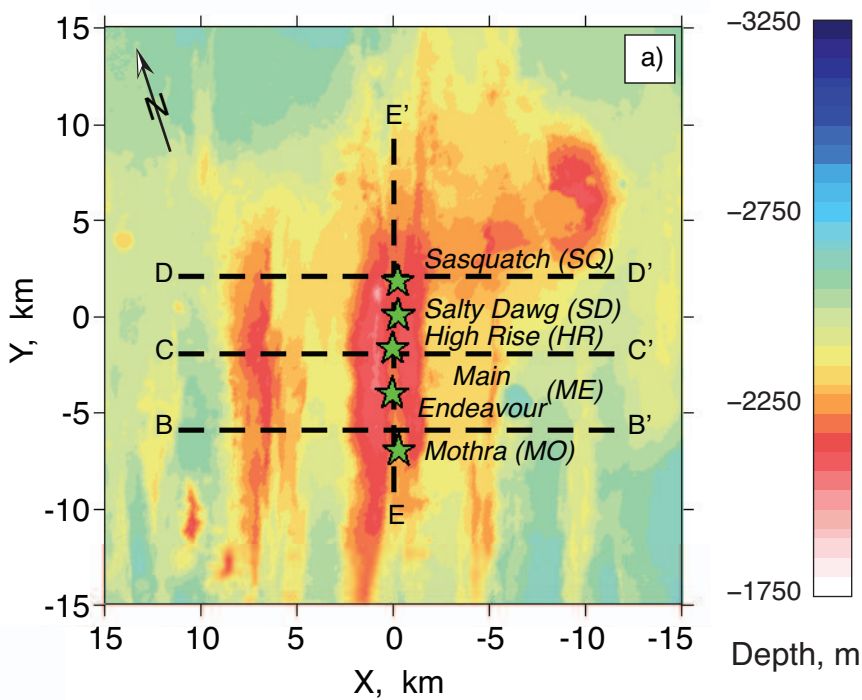




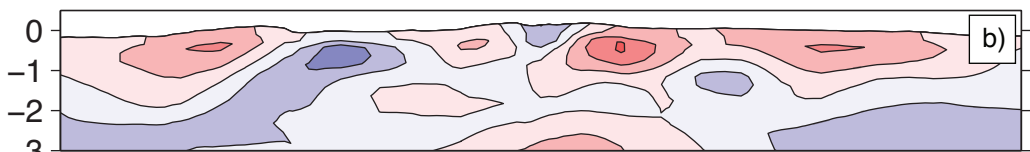




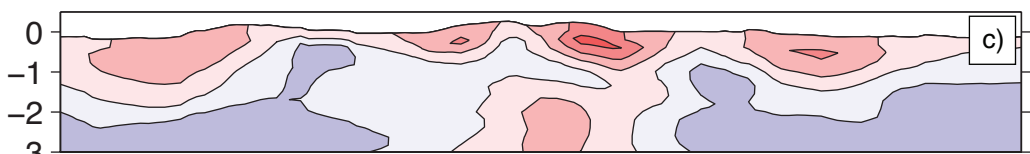




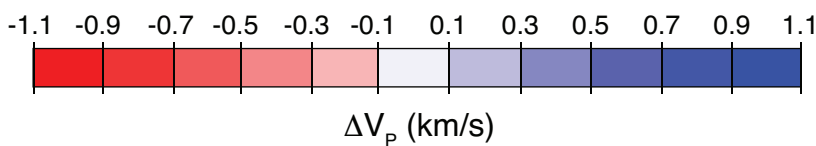
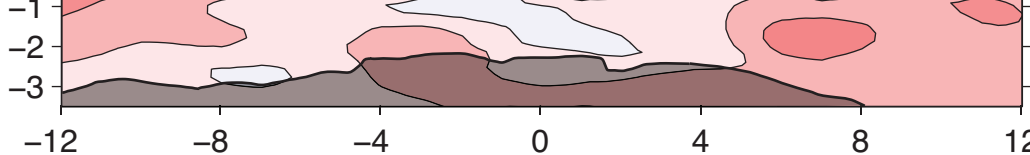
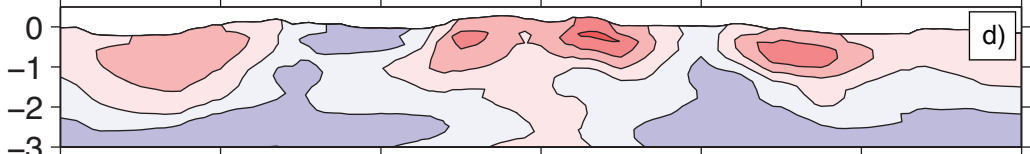
$y = 2$



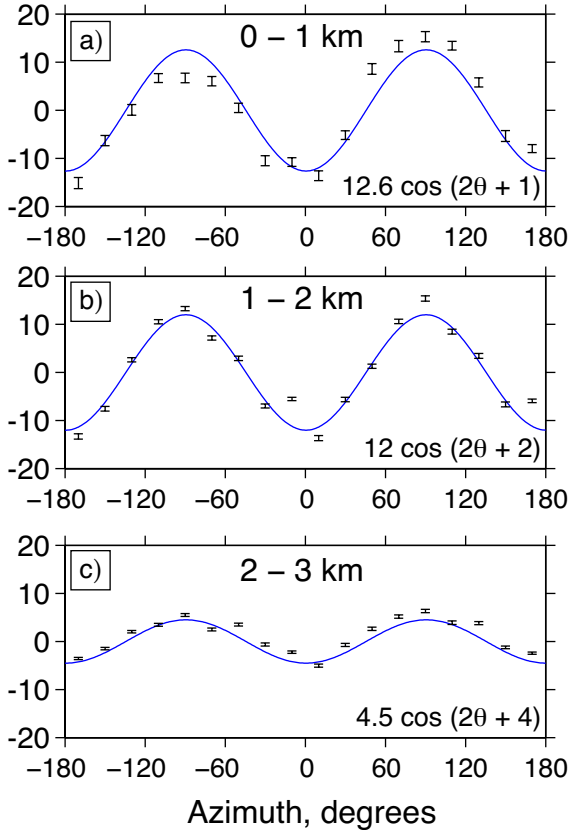
$y = -2$

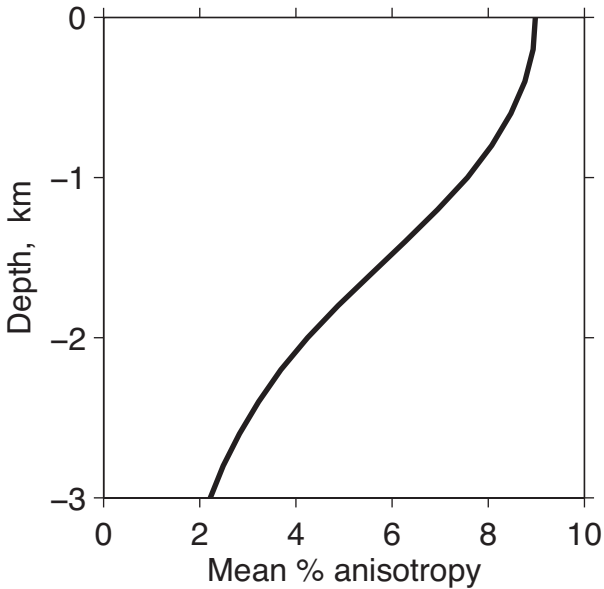


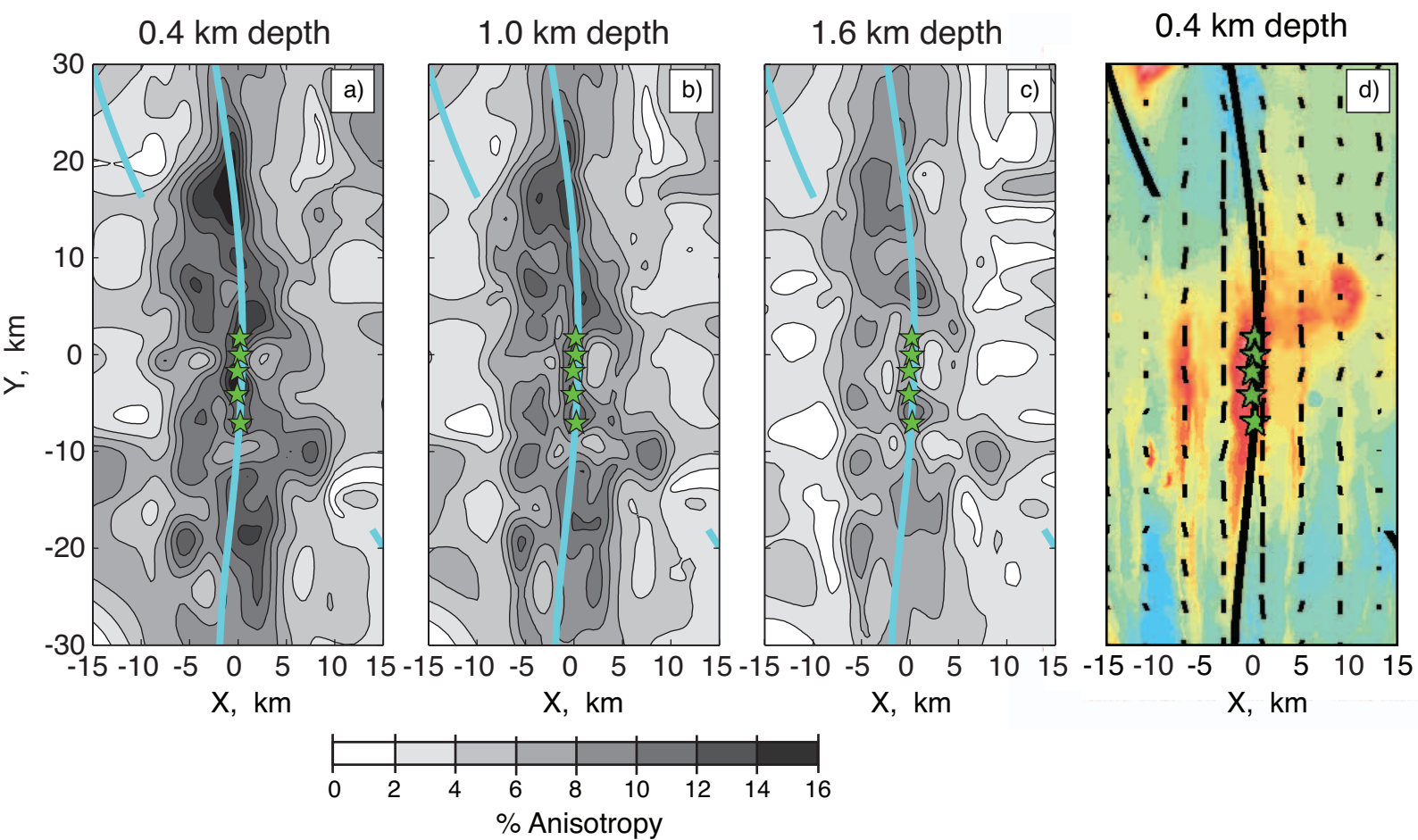
$y = -6$



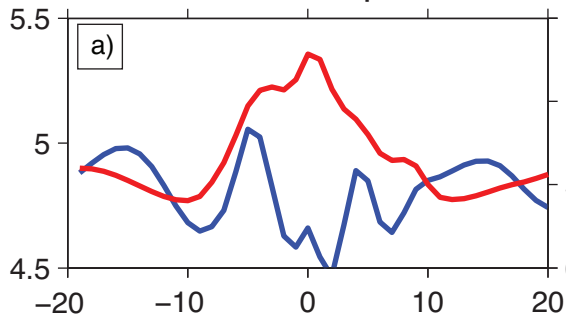
Mean Travel Time Residual (ms)



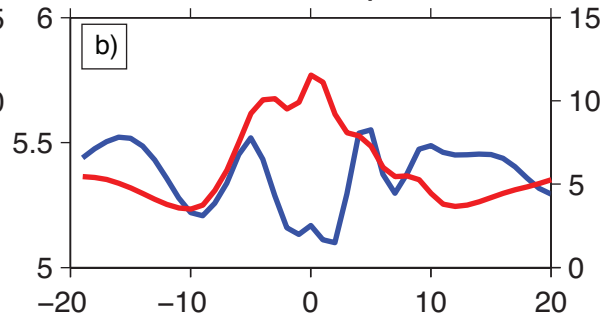




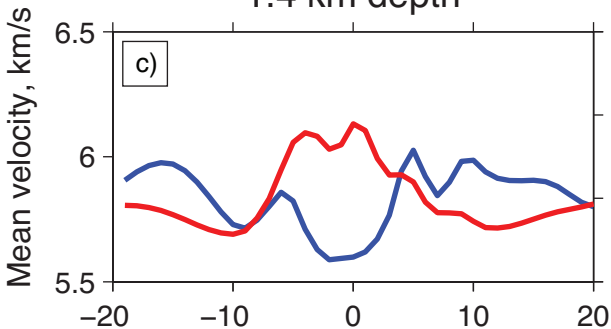
0.6 km depth



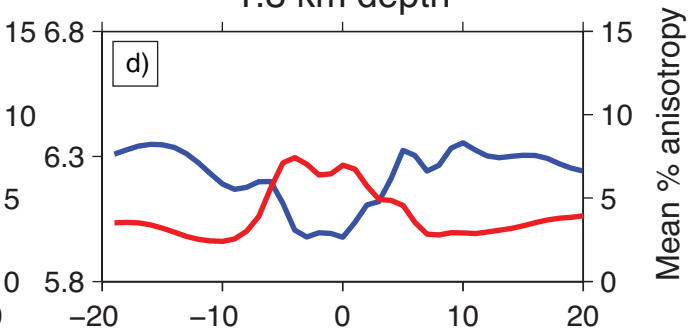
1.0 km depth



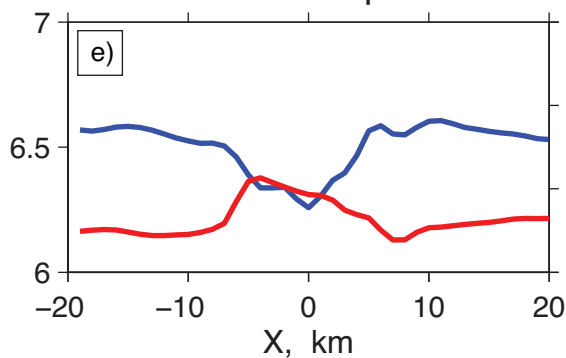
1.4 km depth



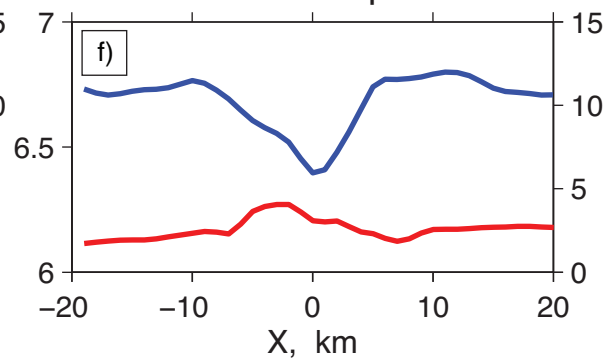
1.8 km depth

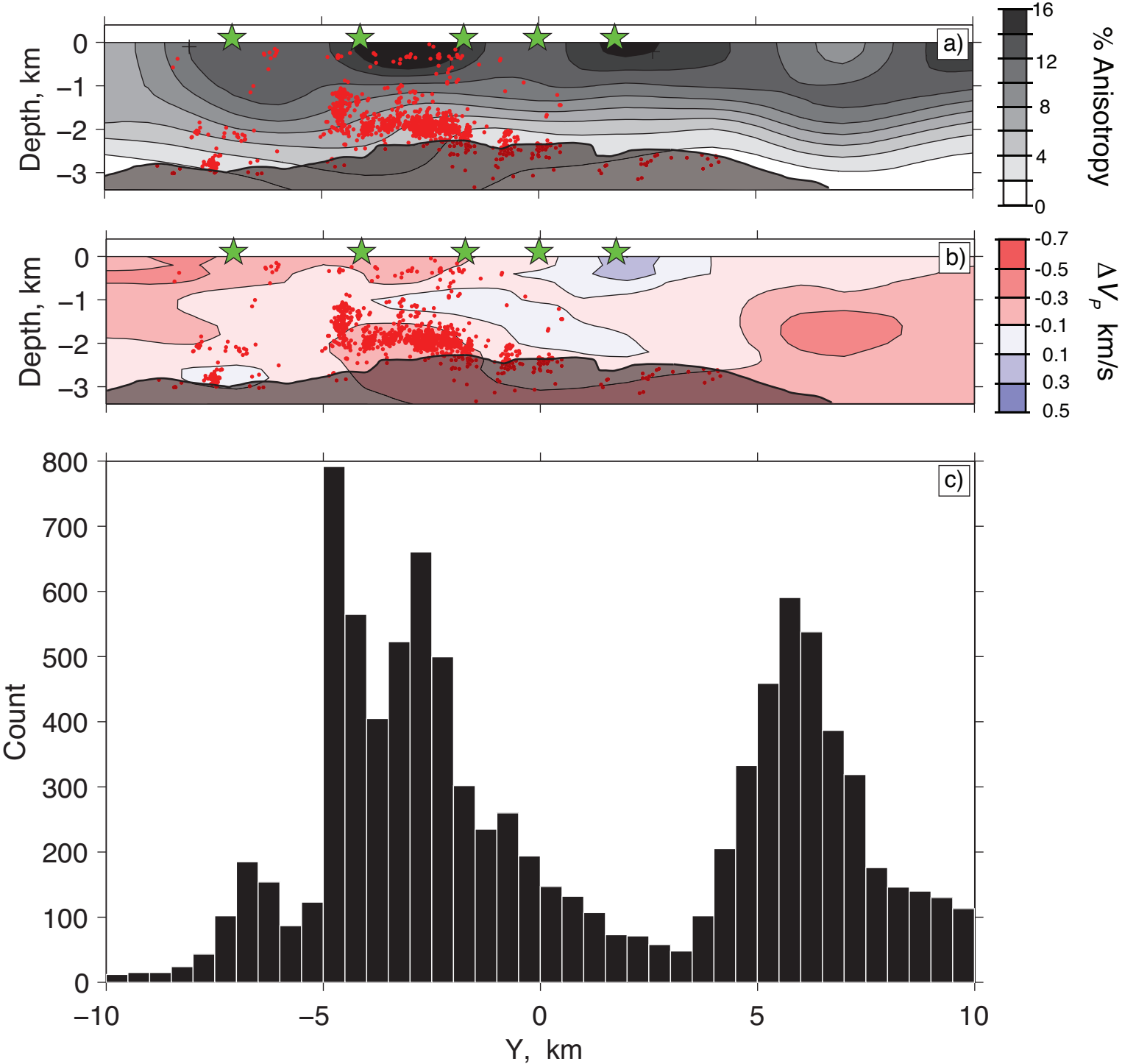


2.2 km depth



2.6 km depth





Upper crustal seismic structure of the Endeavour Segment, Juan de Fuca
Ridge from travel time tomography: Implications for oceanic crustal
accretion

Supplementary Documents

Robert T. Weekly¹, William S.D. Wilcock², Douglas R. Toomey³, Emilie E.E. Hooft³, Eunyoung Kim⁴

(1) Department of Earth and Space Sciences, University of Washington, Box 351310,
Seattle, WA 98195-1310

(2) School of Oceanography, University of Washington, Box 357940, Seattle, WA 98195-
7940

(3) Department of Geological Sciences, University of Oregon, 1272 University of Oregon,
Eugene, OR 97403-1272

(4) School of Earth and Environmental Sciences, Seoul National University, Seoul, Korea,
Republic of

Supplementary Documents

S1. Derivative Weight Sum

To delimit the volume in which our preferred model is well resolved, we analyzed the spatial distribution of ray paths. A spatial measure of the distribution of Pg ray paths within the experiment footprint is given by the derivative weight sum (DWS) [Thurber, 1983; Toomey and Foulger, 1989], which calculates the weighted sum of path lengths influencing each node in the perturbational grid. In short, DWS is a unitless number that describes the influence of ray path density on perturbational grid nodes, and interpretations drawn from results lying below a DWS threshold should be avoided. From inspection of the checkerboard tests (see below), we set a DWS threshold of 10 for masking our models. Selecting a precise value was somewhat subjective and depended on the wavelength of the feature of interest, but DWS increased rapidly inside the minimum contour in most of the model space (Figure S1). Ray path distribution in the upper crust was sparse at the outer edges of the experiment and dense within the centralized crustal grid to depths of ~ 3 km. There was a paucity of ray paths sampling crustal structure below 3 km depth near the central Endeavour segment. This data-limited region of our model resulted from the presence of the AMC located 2 – 3 km beneath the central axial valley [Van Ark *et al.*, 2007], which limited the ranges at which Pg could be easily identified.

S2. Synthetic Isotropic Inversions

To assess the resolution of our results, we used reconstructions of several types of synthetic models. For all synthetic models, we calculated predicted Pg travel-times for the same station-receiver pairs as in our experiment, assigned 10 ms of uncertainty to each arrival time, and inverted the data using the same parameters as in our preferred solutions.

We tested the resolution of isotropic structure by constructing synthetic models of checkerboard pattern velocity anomalies that consisted of 5% velocity perturbations applied to the average one-dimensional velocity structure (solid black line in Figure 4a) and alternated between positive and negative anomalies. All the checkerboard tests show that the tomographic inversion has a tendency to underestimate the magnitude of velocity anomalies even in the best resolved regions.

To evaluate the resolution of segment-scale features, we used columnar checkerboard tiles measuring 10, 15, and 20 km on a side in which the polarity of the perturbations did not alternate with model depth. Figure S2 shows map-view sections of the reconstructed anomalies for the 10-km-by-10-km tiles. The tests demonstrate that structural features on the order of ~10 km in size are generally well resolved between 0.5 and 2.5 km depth. The checkerboard pattern is best recovered between 1 – 2 km depth (Figure S2b), where the tiles are more clearly outlined and the percentage recovery is highest. At these depths, we are able to resolve anomalies near the E-WV and Cobb OSCs with greater resolution and a higher percentage recovery than at depths shallower than 1 km or deeper than 2 km (Figure S2a and S2c, respectively). A broad distribution of ray paths near the intersection of the overlapping limbs enables good recovery of the velocity perturbations, but a lack of ray paths at the distal ends of the OSCs prevents satisfactory recovery of structure in these regions. Similarly, anomalies between 1 km and 2 km depth are better recovered at off-axis distance exceeding ~20 km compared to crustal structure at other depths. We attribute this to the high density and broad azimuthal distribution of P_g ray paths that turn between 1 km and 2 km depth (Figure S1b).

To evaluate the resolution of features located near the more densely-sampled central portion of the segment (Figure S1), we analyzed synthetic checkerboard models with 5-km-by-5-km-by-1-km tiles (Figure S3). Unlike the models of Figure S2, the polarity of the velocity perturbations alternated with depth so we could assess the vertical resolution. Checkerboard anomalies in the upper 1 km are well recovered within 10 km of the ridge but are poorly recovered at larger ranges where they exhibit some horizontal smearing due to poor ray path coverage in the upper crust (Figure S3a). At 1-2 km depth, anomalies are reasonably well recovered near the ridge axis with no evidence for horizontal smearing observed at shallower depths (Figure S3b). Anomalies out to 20 km off-axis are best recovered at these depths (Figure S3). The recovered amplitude of synthetic anomalies at depths greater than ~2 km (Figure S3c) is poor compared to shallower depths, which reflects the small percentage of ray paths turning deeper than ~2 km.

To test the limits of resolution near the hydrothermal fields, we performed inversions of synthetic data from a checkerboard model with 2-km-by-2-km-by-1-km tiles (Figure S4). Recovery of synthetic anomalies indicates that structure near the axial valley is well resolved within the upper 2 km, but the amplitude of the recovered anomalies is higher within the upper 1

km. This synthetic model shows that the resolution of our model is sufficient to resolve features on the scale of the spacing of hydrothermal vents.

S3. Synthetic Anisotropic Inversions

We conducted a series of synthetic models to evaluate the anisotropic component of our inversions. First, to investigate the tradeoff between isotropic and anisotropic structure in the inversion, we considered a synthetic model in which the isotropic component was the average vertical velocity structure of the preferred model (solid line, Figure 4a) and the amplitude of ridge-parallel anisotropy decreased from 5% at the seafloor to 0% at 4 km depth (dashed line in Figure S5). Figures S5 and S6-c show the difference between the starting model and the synthetic model.

The horizontally-averaged recovered anisotropic signal in this inversion is smaller than in the starting model at all depths (Figure S5) and the magnitude of the anisotropic signal tends to decrease off-axis (Figure S6a-c). In order to assess whether this effect might produce the large decrease in the magnitude of anisotropy observed in our preferred model within 5 to 10 km of the ridge axis (Figure 10-11), we conducted a second synthetic anisotropic inversion that was identical to the first except that the magnitude of anisotropy was doubled within 5 km of the ridge axis. Figure S6d-f shows the recovered magnitude of anisotropy at three depths.

Figure S7 shows the change in the average percentage of anisotropy off-axis at different depths for the preferred model and for the two synthetic inversions. It is clear that the synthetic inversion with higher anisotropy near the ridge axis more closely reproduces the change in the magnitude of anisotropy seen off-axis than the model with constant anisotropy. Indeed, it appears that a doubling of anisotropy near the ridge axis is insufficient to reproduce the preferred inversion. Thus, we infer that while the inversions will tend to underestimate the magnitude of anisotropy, particularly well off-axis, the large decrease in the magnitude of anisotropy off-axis in the preferred model is a real effect. The preferred inversions also shows significantly larger along-axis variations in the magnitude of anisotropy than the synthetic inversion of Figure S6d-f, so we infer that along-axis variations in the magnitude of anisotropy are required by the data.

To evaluate the ability of the inversions to resolve variations in the magnitude of anisotropy, we used synthetic models with a checkerboard patterns of anisotropy in which the fast direction is everywhere parallel to the ridge axis but the magnitude of anisotropy varies.

Figure S8 shows the recovery for a model with 5-km-by-5-km columnar tiles and a magnitude that in half of the tiles decreased from 5% at the seafloor to 0% at 4 km depth (dashed line in Figure S5) and is twice this in the other half. The results show that the variations in the relative magnitude of anisotropy is well recovered within 10 km of the ridge axis but that the amplitude is everywhere somewhat underestimated. At distances greater than 10 km off axis (i.e., outside the region of the intermediate grid), anisotropy magnitude variations on this length scale are not well resolved.

To evaluate the ability of the inversions to resolve variations in the orientation of the fast direction of anisotropy, we used synthetic models with checkerboard patterns of anisotropy in which the magnitude was constant throughout the model but the fast direction varied. Figure S9 shows the recovery for two models with 10-km-by-10-km columnar tiles and a fast direction that is rotated by 90° and 45°, respectively, between adjacent tiles. Recovery of the synthetic data shows that variations in the orientation of anisotropy near the central portion of the experiment are well resolved, however, the synthetic models are not as well recovered near the margins of the experiment. In these regions, the recovered azimuths are often intermediate between the values of adjacent tiles. We attribute this lack of fine-scale resolution to the relatively poor azimuthal distribution of ray paths near the edges of the experiment.

Supplementary References

- Thurber, C. H. (1983), Earthquake locations and three-dimensional crustal structure in the Coyote Lake Area, Central California, *J. Geophys. Res.*, *88*, 8226-8236, doi:10.1029/JB088iB10p08226.
- Toomey, D. R., and G. R. Foulger (1989), Tomographic inversion of local earthquake data from the Hengill-Grensdalur Central Volcano Complex, Iceland, *J. Geophys. Res.*, *94*, 17497-17510, doi:10.1029/JB094iB12p17497.
- Van Ark, E. M., R. S. Detrick, J. P. Canales, S. M. Carbotte, A. J. Harding, G. M. Kent, M. R. Nedimovic, W. S. D. Wilcock, J. B. Diebold, and J. M. Babcock (2007), Seismic structure of the Endeavour Segment, Juan de Fuca Ridge: Correlations with seismicity and hydrothermal activity, *J. Geophys. Res.*, *112*(B2), B02401, doi:10.1029/2005jb004210.

Supplementary Document Figure Captions

- S1) Map-view sections of the derivative weight sum (DWS) at (a) 0.5 km, (b) 2.0 km, and (c) 3.5 km depth contoured at 10, 100 and 1000 to show the relative density of rays.
- S2) Map-view slices at (a) 0.4 km, (b) 1.4 km, and (c) 2.4 km depths showing results from synthetic isotropic velocity checkerboard tests for columnar 10-km-by-10-km tiles. Velocity perturbations were $\pm 5\%$ from the preferred isotropic model and perturbations did not vary with depth. Green stars show the locations of vent fields. Solid black lines show the traces of the West Valley, Endeavour, and Northern Symmetric segments. The color contours show the percent recovery of the *P*-wave perturbation with a contour interval of 20%.
- S3) Map-view slices at (a) 0.4 km, (b) 1.4 km, and (c) 2.4 km depths showing results from synthetic isotropic velocity checkerboard tests for 5-km-by-5-km-by-2-km tiles. The same plotting conventions are used as for Figure S2.
- S4) Map-view slices taken at (a) 0.4 km and (b) 1.4 km depths and (c) vertical cross-section through the vent fields ($X = 0$ km) showing results from synthetic isotropic velocity checkerboard tests for 2-km-by-2-km-by-1-km tiles. The same plotting conventions are used as for Figure S2.
- S5) One-dimensional percent anisotropy structure for a synthetic model used to calculate travel times (dashed line) and the vertical average of the model recovered from the inversion in a region extending 10 km to either side of the ridge axis and from $Y = -20$ km to $Y = 20$ km (solid line).
- S6) Map-view slices at 0.4 km, 1.2 km and 2 km depth showing the magnitude of anisotropy contoured at 1% intervals for two synthetic inversions. (a–c) Results for the inversion shown in Figure S5 in which the anisotropy in the model used to calculate synthetic travel times varies from 5% at the seafloor to 0% at 4 km depth. (d–f) Results for an

inversion in which the model used to calculate synthetic travel times is the same as before except the magnitude of anisotropy is doubled within 5 km of the ridge axis ($-5 \text{ km} < X < 5 \text{ km}$). The vent fields (green stars) and traces of the segments (bold cyan lines) are also shown.

S7) Plots showing the change in average magnitude of anisotropy as a function of off-axis range for the preferred anisotropic model discussed in the text (black), the synthetic inversion of Figure S6a-c with horizontally invariant anisotropy (red) and the synthetic inversion of Figure S6d-f with the magnitude of anisotropy doubled within 5 km of the ridge axis (blue). Note that the shape of the curves for the second synthetic inversion more closely resembles that for the preferred isotropic model, indicating that the off-axis decrease in anisotropy is well-resolved.

S8) Map view slices of the magnitude of anisotropy contoured at 1% intervals at 0.4 km, 1.0 km and 1.6 km depth for the recovery of a synthetic anisotropic checkerboard model in which the fast direction was oriented along the ridge axis (Y axis). The magnitude of anisotropy varied in alternate 5-km-by-5-km checkers from 10% and 5%, respectively at the seafloor to 0% at 4 km depth following the profile shown by a dashed line in Figure S5. Note that structure is well resolved within 10 km of the axis but that the amplitude of the anisotropy is underestimated.

S9) Map-view slices of the orientation of anisotropy taken at 0.4 km depth for the recovery of synthetic anisotropic checkerboard models for 10-km-by-10-km columnar tiles in which the orientation of seismic anisotropy is perturbed by (a) 90° and (b) 45° . Solid black lines show the orientation and relative magnitude of the fast direction of anisotropy on a 4-km-by-4-km grid. A tick of length 4 km would represent 100% recovery of the anisotropy magnitude. The vent fields (green stars) and traces of the segments (bold black lines) are also shown.

Supplementary material for manuscript 2013GC005159

Upper crustal seismic structure of the Endeavour Segment, Juan de Fuca Ridge from travel time tomography: Implications for oceanic crustal accretion

Robert T. Weekly (Dept. of Earth and Space Sciences, Univ. of Washington, Seattle, WA)

William S.D. Wilcock (School of Oceanography, Univ. of Washington, Seattle, WA)

Douglas R. Toomey (Dept. of Geological Sciences, Univ. of Oregon, Eugene, OR)

Emilie E.E. Hooft (Dept. of Geological Sciences, Univ. of Oregon, Eugene, OR)

Eunyoung Kim (School of Earth and Environmental Sciences, Seoul National University, Seoul, Korea, Republic of)

Geochem. Geophys. Geosyst., doi:10.1029/2013GC005159, 2013

Introduction

The Supplementary Information includes: (1) a document that describes the lateral resolution of our isotropic and anisotropic velocity models for the Endeavour Segment, Juan de Fuca Ridge, and (2) nine figures that support the documentation.

1. 2013GC005159_suppdoc.docx - Supplementary document text

This document includes text and figures pertaining to analysis of raypath density and resolution tests for our isotropic and anisotropic velocity models for the Endeavour Segment.

2. FIGS1_2013GC005159.eps - Supplementary Figure S1

A map of Pg ray path density within the experiment footprint

3. FIGS2_2013GC005159.eps - Supplementary Figure S2

Coarse-scale Isotropic Checkerboard Resolution Test

4. FIGS3_2013GC005159.eps - Supplementary Figure S3

Intermediate-scale Isotropic Checkerboard Resolution Test

5. FIGS4_2013GC005159.eps - Supplementary Figure S4

Fine-scale Isotropic Checkerboard Resolution Test

6. FIGS5_2013GC005159.eps - Supplementary Figure S5

Comparison of recovered synthetic 1-D anisotropic structure

7. FIGS6_2013GC005159.eps - Supplementary Figure S6

Segment-scale Anisotropic Resolution Test

8. FIGS7_2013GC005159.eps - Supplementary Figure S7

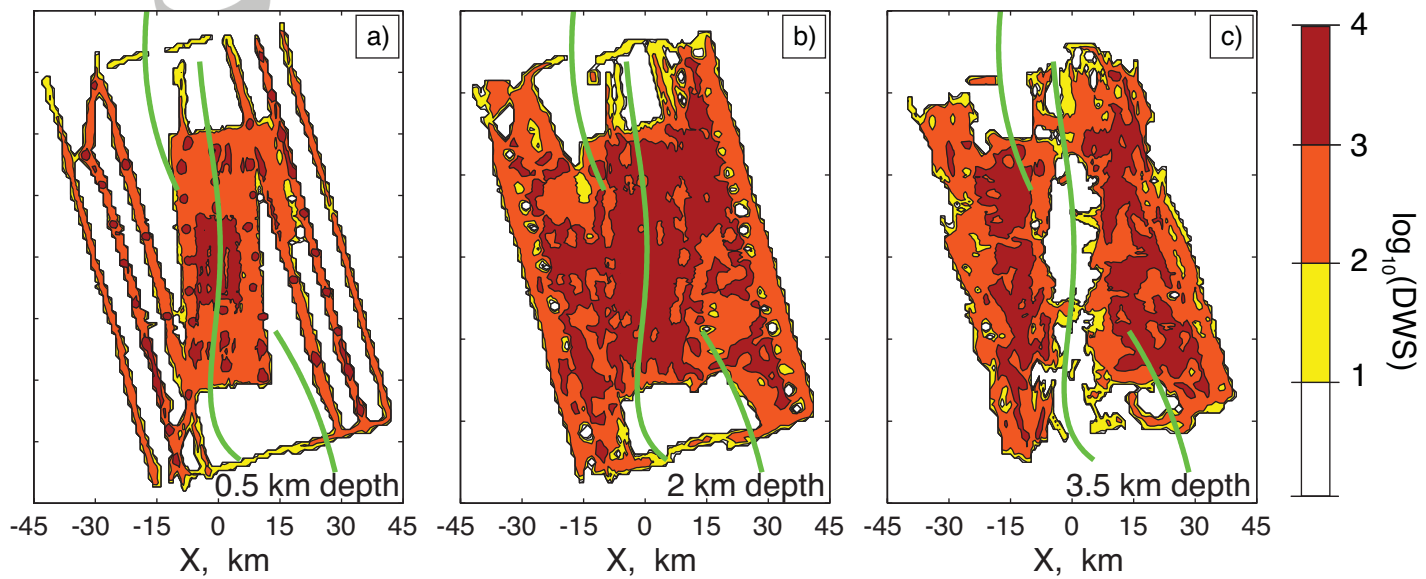
Off-axis Anisotropic Resolution Test

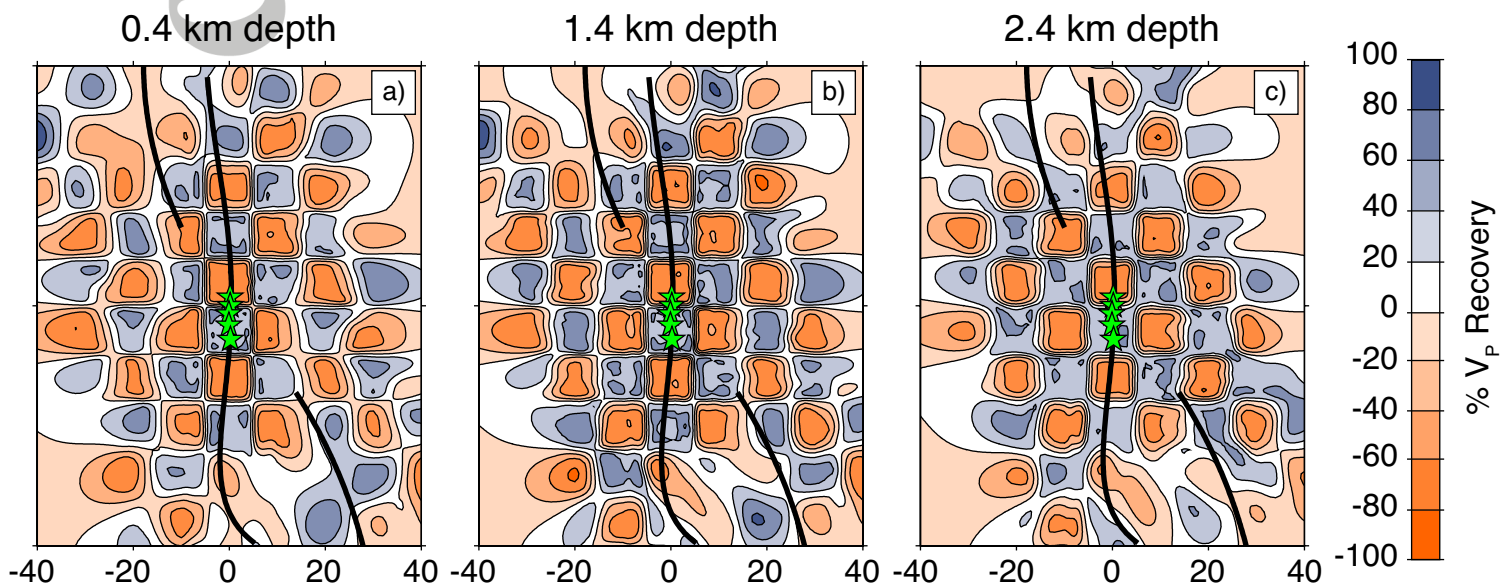
9. FIGS8_2013GC005159.eps - Supplementary Figure S8

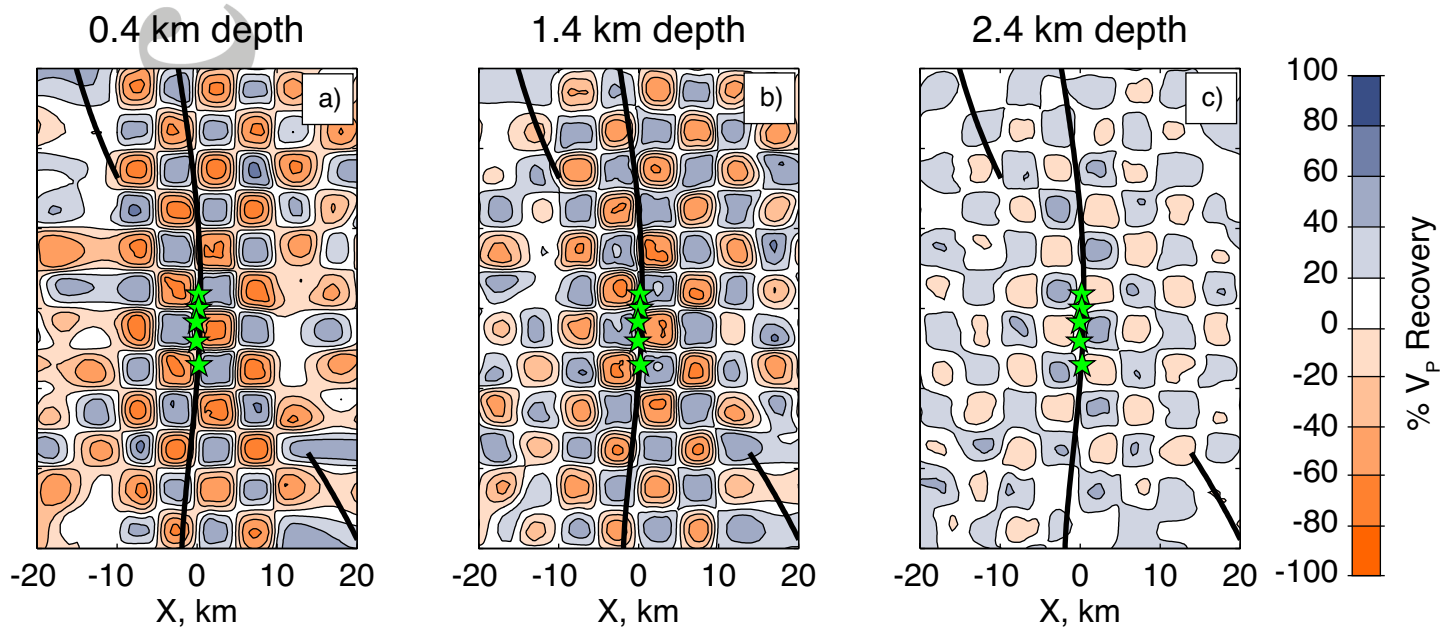
Anisotropic Percentage Checkerboard Resolution Test

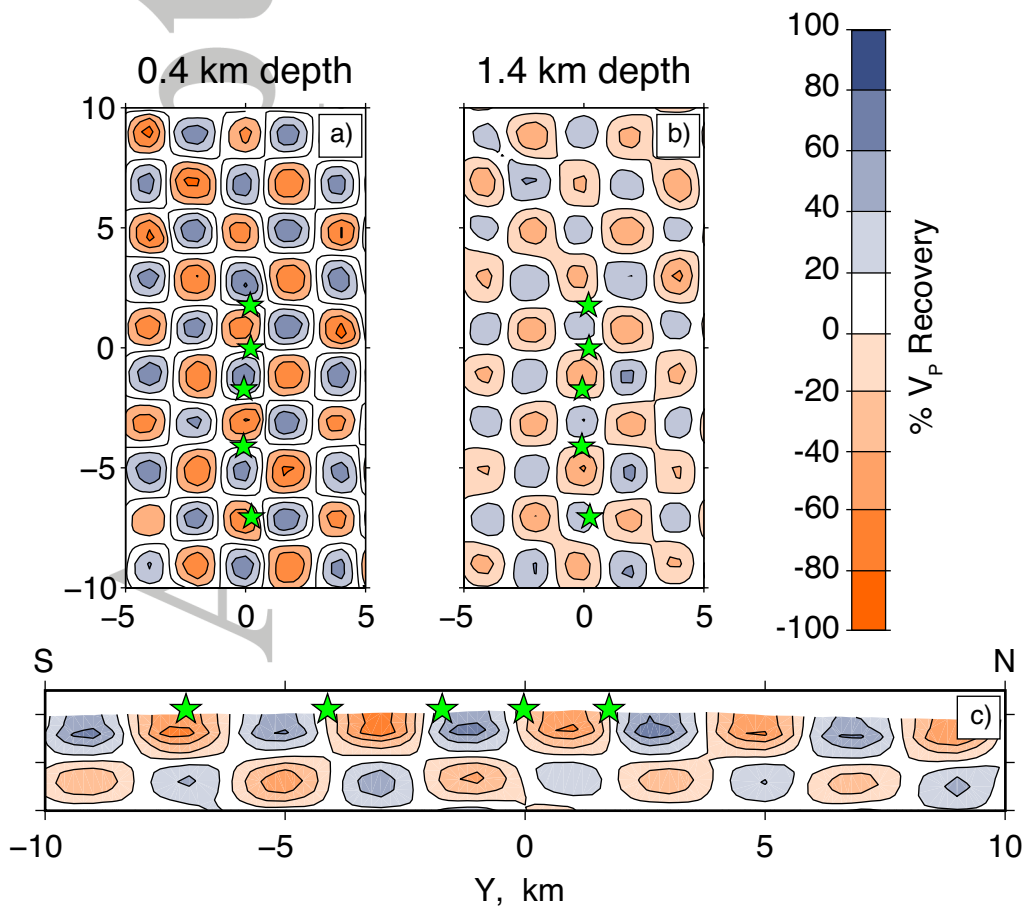
10. FIGS9_2013GC005159.eps - Supplementary Figure S9
Anisotropic Azimuth Checkerboard Resolution Test

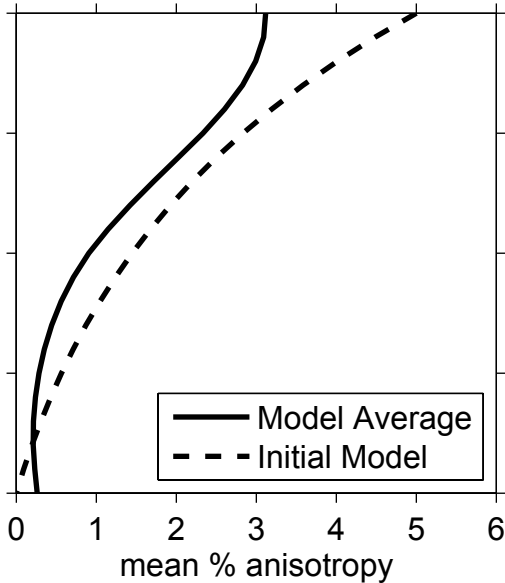
Accepted Article

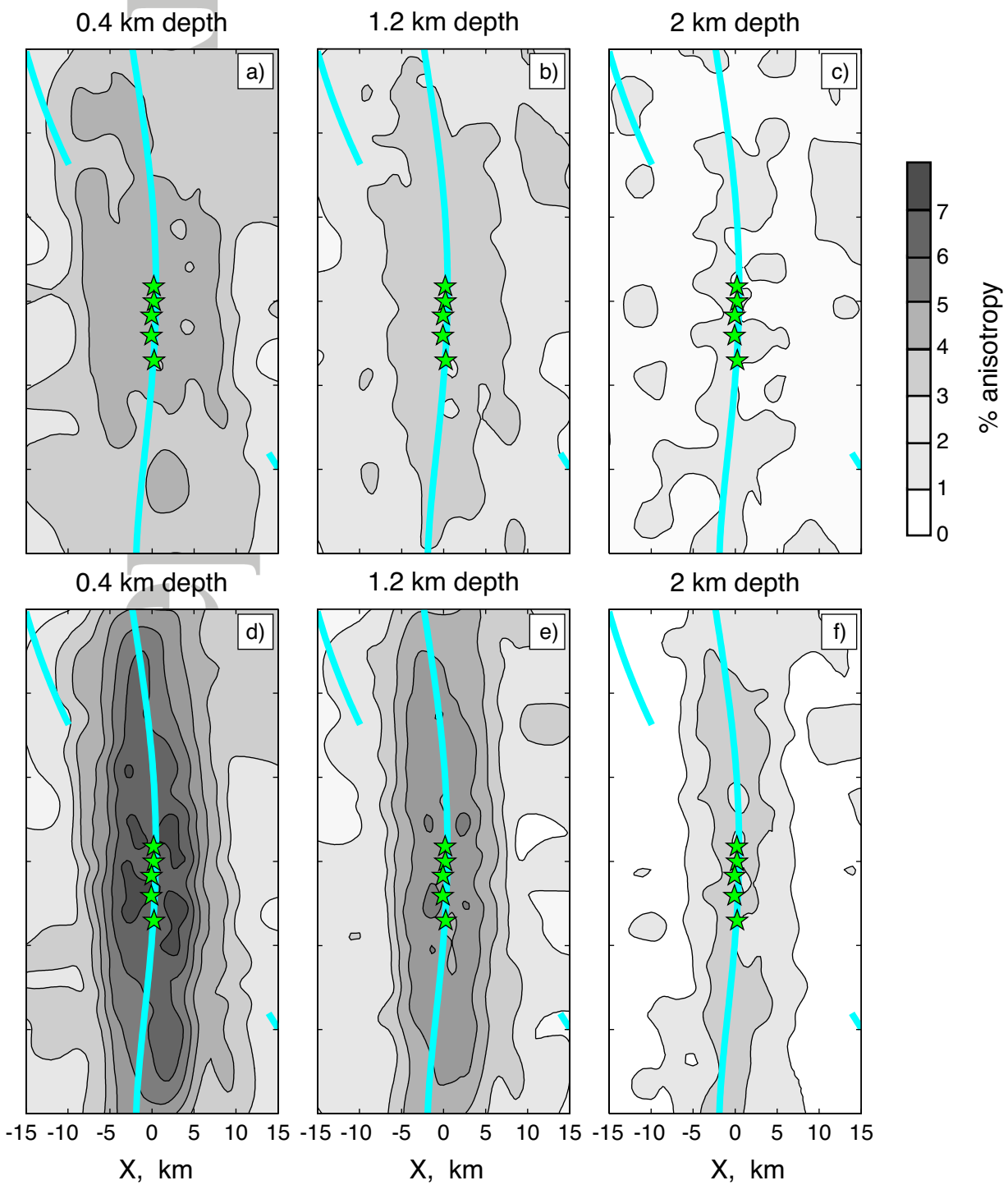




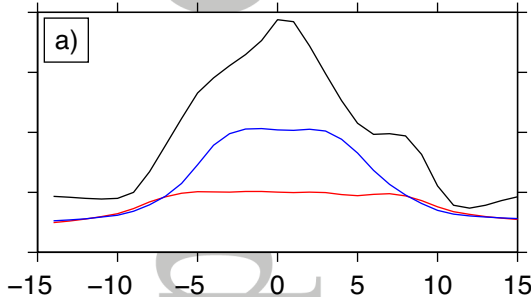




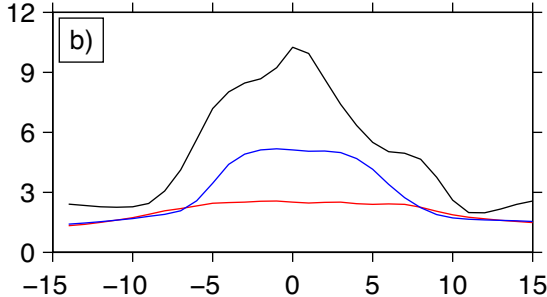




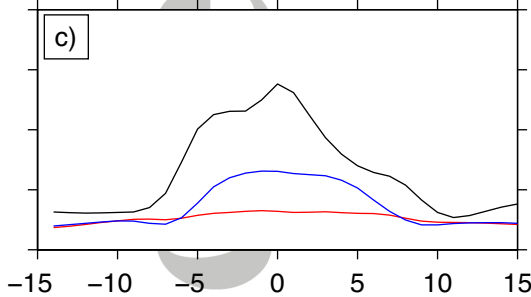
0.6 km depth



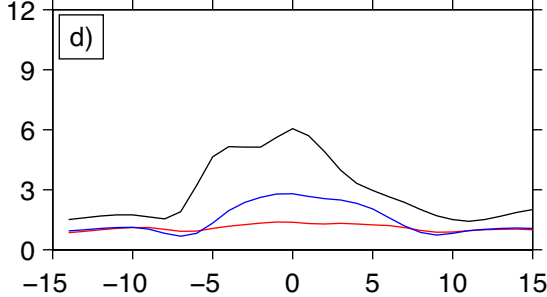
1.0 km depth



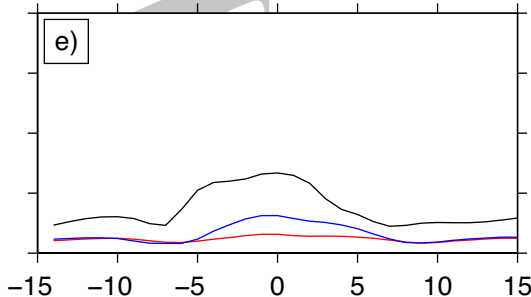
1.4 km depth



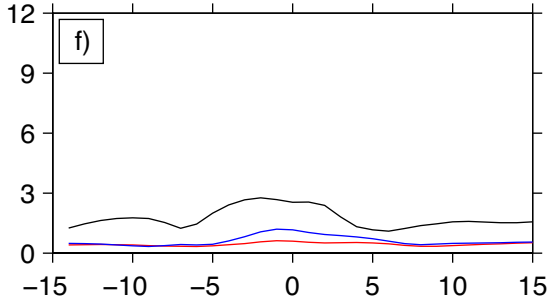
1.8 km depth



2.2 km depth



2.6 km depth



X, km

X, km

